nature metabolism

ARTICLES

https://doi.org/10.1038/s42255-022-00588-8

Cancer cells depend on environmental lipids for proliferation when electron acceptors are limited

Zhaoqi Li[1,2,13], Brian W. Ji[3,4,13], Purushottam D. Dixit[3,5,6,7,8,13], Konstantine Tchourine[3], Evan C. Lien[1], Aaron M. Hosios[1,2], Keene L. Abbott[1,2], Justine C. Rutter[1,9], Anna M. Westermark[1], Elizabeth F. Gorodetsky[1], Lucas B. Sullivan[1,10], Matthew G. Vander Heiden[1,2,11] ✉ and Dennis Vitkup[3,12] ✉

Production of oxidized biomass, which requires regeneration of the cofactor NAD⁺, can be a proliferation bottleneck that is influenced by environmental conditions. However, a comprehensive quantitative understanding of metabolic processes that may be affected by NAD⁺ deficiency is currently missing. Here, we show that de novo lipid biosynthesis can impose a substantial NAD⁺ consumption cost in proliferating cancer cells. When electron acceptors are limited, environmental lipids become crucial for proliferation because NAD⁺ is required to generate precursors for fatty acid biosynthesis. We find that both oxidative and even net reductive pathways for lipogenic citrate synthesis are gated by reactions that depend on NAD⁺ availability. We also show that access to acetate can relieve lipid auxotrophy by bypassing the NAD⁺ consuming reactions. Gene expression analysis demonstrates that lipid biosynthesis strongly anti-correlates with expression of hypoxia markers across tumor types. Overall, our results define a requirement for oxidative metabolism to support biosynthetic reactions and provide a mechanistic explanation for cancer cell dependence on lipid uptake in electron acceptor-limited conditions, such as hypoxia.

Many proliferating cancer cells incorporate biomass precursors such as amino acids, nucleic acids and lipids from their environment[1–4]. Nonetheless, nutrient and oxygen availability vary across tumors[5–7] and these environmental differences can govern the functioning of metabolic pathways used to support proliferation[5,8,9]. Metabolism of nutrients to produce oxidized biomass precursors requires regeneration of the cofactor NAD⁺ to serve as an electron acceptor, and there is accumulating evidence that NAD⁺ availability can be limiting for biomass production and cell proliferation in vivo and in vitro[10–17]. NAD⁺ regeneration has been shown to be important for the biosynthesis of aspartate, nucleotides and serine[11,13,17–19]. Conversely, synthesis of other molecules such as select fatty acids has been proposed to support proliferation by enabling NAD⁺ regeneration[20]. However, a systems-level quantitative analysis of the NAD⁺ consumption costs required to produce various biomass components is currently missing.

Lipids are essential components of cellular biomass, and de novo lipid biosynthesis is generally considered to be a reductive process. The production of reducing equivalents in the form of NADPH has long been known to be a prerequisite for fatty acid synthesis[21]. Notably, the desaturation of fatty acids requires NAD(P)H and regenerates NAD(P)⁺, although these reactions also consume molecular oxygen[20,22]. Lipid metabolism is also connected with cellular energetics. The synthesis of free fatty acids is controlled by the energy-sensing AMP-activated protein kinase, as fatty acid synthesis requires ATP, while fatty acid oxidation can be an important source of energy[23,24]. Previous studies have found that under conditions of oxygen limitation cancer cell proliferation and survival become dependent on access to exogenous lipids, suggesting that this phenotype is driven by the requirement for oxygen in energy generation and/or lipid desaturation reactions[25–28]. However, oxygen also serves as a terminal electron acceptor used to regenerate NAD⁺, and this requirement can substantially exceed the demand for lipid desaturation reactions and ATP generation at least in some contexts[29]. Cells respond to oxygen limitation via stabilization of hypoxia inducible factor (HIF1α)[30], which promotes a shift in carbon source for lipogenic citrate from glucose oxidation to glutamine reduction[31–34]. Nevertheless, in all known instances where reductive glutamine metabolism is used to generate fatty acids, the rate of fatty acid synthesis from the reductive pathway is lower than the rate from oxidative glucose metabolism, but why this is the case, and what ultimately governs the rates of lipogenic citrate production from different carbon sources remains an open question.

In this study, we combined computational and experimental approaches to demonstrate that de novo synthesis of lipogenic citrate incurs a substantial NAD⁺ consumption cost. We then investigated the biochemical and regulatory mechanisms underlying the dependency of cancer cell proliferation on exogenous lipids in hypoxia or when the electron transport chain (ETC) is inhibited in normoxia. We first explored this question by enabling alternative pathways for NAD⁺ regeneration and by providing nutrients that can bypass or relieve the NAD⁺ requirement for de novo lipid synthesis. We then performed kinetic isotope tracing experiments to identify specific reactions that gate lipogenic citrate synthesis from

[1]Koch Institute for Integrative Cancer Research, Massachusetts Institute of Technology, Cambridge, MA, USA. [2]Department of Biology, Massachusetts Institute of Technology, Cambridge, MA, USA. [3]Department of Systems Biology, Columbia University, New York, NY, USA. [4]Physician-Scientist Training Pathway, Department of Medicine, University of California, San Diego, San Diego, CA, USA. [5]Department of Physics, University of Florida, Gainesville, FL, USA. [6]University of Florida Genetics Institute, University of Florida, Gainesville, FL, USA. [7]Department of Chemical Engineering, University of Florida, Gainesville, FL, USA. [8]University of Florida Cancer Center, University of Florida, Gainesville, FL, USA. [9]Health Sciences and Technology (HST) and Harvard/MIT MD-PhD Program, Harvard Medical School, Boston, MA, USA. [10]Human Biology Division, Fred Hutchinson Cancer Research Center, Seattle, WA, USA. [11]Dana-Farber Cancer Institute, Boston, MA, USA. [12]Department of Biomedical Informatics, Columbia University, New York, NY, USA. [13]These authors contributed equally: Zhaoqi Li, Brian W. Ji, Purushottam D. Dixit. ✉e-mail: mvh@mit.edu; dv2121@cumc.columbia.edu

glucose and glutamine when electron acceptors are limited. We also investigated regulatory interactions that may influence the rewiring of lipid metabolism in hypoxia and when the ETC is inhibited. Finally, we analyzed the expression correlations of fatty acid synthesis and uptake pathways with hypoxia markers across a large collection of tumors. Together, our experiments reveal how NAD^+ availability can govern the rate of lipid biosynthesis, and thus provide a mechanistic biochemical explanation for the lipid auxotrophy of cancer cells in conditions where electron acceptors are limited.

Results

Computational analysis predicts a substantial NAD^+ consumption cost of lipogenic acetyl-CoA. NAD^+ availability can be limiting for cell proliferation in many contexts[10–17]. To quantify the potential requirements for NAD^+ regeneration to support biomass synthesis and cell proliferation, we used a genome-scale stoichiometric model of human cell metabolism[35]. We applied flux balance analysis (FBA)[36] to calculate the minimal levels of NAD^+ consumption required for the de novo synthesis of major biomass components (Methods). To accomplish this, we first pruned the original genome-scale model to retain key metabolic reactions that are likely to be involved in biomass production[37,38]. The automatic pruning procedure was constrained such that the resulting models approximated experimentally measured metabolic exchange fluxes for each of the NCI-60 cell lines[3]. Each of the resulting FBA models comprised ~600 reactions that allowed the models to support biomass synthesis. We then used the obtained FBA models to estimate the minimum level of NAD^+ consumption needed for the production of lipogenic acetyl-CoA from glucose and glutamine, as well as for the synthesis of nucleotides and nonessential amino acids (Methods). The modeling was able to recapitulate previous findings that aspartate, serine and nucleotides all have an associated NAD^+ cost of production that can be limiting for proliferation (Fig. 1a)[11,13,17–19]. Surprisingly, the computational model also predicted a substantial NAD^+ cost of lipid synthesis (Fig. 1a). In mammalian cells, lipogenic acetyl-CoA is reported to be synthesized either through glucose oxidation[1,39–41], which requires NAD^+ for glycolysis, the pyruvate dehydrogenase (PDH) reaction and tricarboxylic acid (TCA) cycle reactions. Alternatively, lipogenic acetyl-CoA can be synthesized through reductive carboxylation of glutamine-derived alpha-ketoglutarate (αKG), where the production of αKG from glutamine-derived glutamate either directly consumes NAD^+ or indirectly requires access to electron acceptors downstream of any transamination reaction[11,39,42–44] (Fig. 1b). While the synthesis of fatty acids or sterols from acetyl-CoA is a reductive process that requires NADPH, the computational analysis predicted that de novo lipogenic acetyl-CoA synthesis, either from glucose or from glutamine, incurs a substantial NAD^+ consumption cost that could exceed the demand for production of other major biomass precursors (Fig. 1a).

To test the model prediction that access to NAD^+ can be limiting for lipid synthesis, we first examined whether increasing de novo lipid synthesis increases the rate of NAD^+ regeneration via mitochondrial respiration, as this is a major route to regenerate NAD^+ and support cellular oxidation reactions. To that end, we cultured cancer cells in standard normoxic conditions in medium with serum that was chemically stripped of lipids using *n*-butanol and diisopropyl ether extraction (−lipids), or in the same medium with lipids (0.02 μg ml^{-1} arachidonic acid and 0.1 μg ml^{-1} each of linoleic, linolenic, myristic, oleic, palmitic and stearic acids, and 2.2 μg ml^{-1} cholesterol) added back (+lipids)[1,45]. As previously demonstrated, proliferation rates were similar in the presence or absence of exogenous lipids (Fig. 1c,d)[1]; however, cells cultured in the absence of exogenous lipids had increased palmitate synthesis rates and increased sensitivity to fatty acid synthase (FASN) inhibition (Extended Data Fig. 1a,b). These data are consistent with a requirement for increased de novo lipogenesis in lipid-depleted conditions. Next, we reasoned that if increased NAD^+ regeneration is necessary to support upregulated lipid synthesis, oxygen consumption may also increase[25,28]. Indeed, the oxygen consumption rate (OCR) increased in cells cultured in lipid-depleted conditions, and this elevated OCR was sensitive to the mitochondrial ETC inhibitors rotenone and antimycin A (Fig. 1e,f and Extended Data Fig. 1c,d). The difference in OCR between lipid-rich and lipid-depleted conditions is consistent with our computational estimations of the NAD^+ recycling need for lipid biosynthesis, which was inferred from the cells' lipid composition and proliferation rates (Supplementary Methods). Both the experimental and computational results suggest that up to 30% of the overall oxygen uptake in cells primarily relying on de novo lipid biosynthesis is associated with the regeneration of NAD^+ required for lipid production. This oxygen uptake requirement is about an order of magnitude higher than the oxygen consumption necessary for fatty acid desaturation reactions (Supplementary Methods). Interestingly, the increased OCR in lipid-depleted conditions was rapidly reversible (within minutes) upon re-addition of lipids (Extended Data Fig. 1e).

Previous work has attributed the increased OCR associated with upregulation of lipid synthesis to increased ATP demand driving oxidative phosphorylation, as well as to an increased oxygen consumption for desaturating fatty acids[25,28]. The finding that OCR is sensitive to inhibitors of the mitochondrial ETC (Extended Data Fig. 1c,d) argues that the use of molecular oxygen for desaturation reactions cannot fully explain the observed increase in OCR. Furthermore, when the stearyl-CoA desaturase 1 (SCD1) inhibitor A939572 was added to cells, we observed relatively minor changes in OCR compared to ones observed with mitochondrial ETC inhibitors (Extended Data Fig. 1f). These results suggest that the increased mitochondrial OCR could reflect both an increased demand for ATP and for NAD^+ regeneration as an explanation for upregulated mitochondrial respiration.

NAD^+ regeneration promotes cancer cell proliferation in lipid-free conditions. To investigate whether NAD^+ regeneration is limiting for lipid synthesis and substantially contributes to the increased OCR observed in lipid-depleted conditions, we first considered the relationship between de novo lipid synthesis and hypoxia. Previous studies have implicated hypoxia in conferring lipid auxotrophy in vivo and in vitro[25,46]. These studies explored the possibility that hypoxia either directly limits oxygen availability for lipid desaturation reactions or downregulates citrate production through pyruvate dehydrogenase kinase 1 (PDK1)-mediated inhibition of PDH[47,48], which catalyzes pyruvate conversion to acetyl-CoA[26,49–54]. However, hypoxia also reduces NAD^+ regeneration via mitochondrial electron transport and therefore decreases the NAD^+/NADH ratio[5,8,30]. Consistent with previous findings, culturing cells in the absence of exogenous lipids resulted in decreased proliferation in hypoxic but not normoxic conditions[25,46] (Fig. 2a and Extended Data Fig. 2a). Exposing cells to inhibitors of mitochondrial electron transport in normoxia similarly decreased cell proliferation (Fig. 2b and Extended Data Fig. 2b,c). Culturing cells with phenformin, a mitochondrial complex I inhibitor[55], resulted in reduced palmitate synthesis and decreased proliferation in the absence of exogenous lipids (Fig. 2b and Extended Data Figs. 1b and 2b,c); other mitochondrial ETC inhibitors, such as rotenone and antimycin A, had similar effects (Fig. 2c and Extended Data Fig. 2b,c). Notably, neither phenformin nor antimycin A altered PDH (S293) phosphorylation, suggesting that their effects on reducing cell growth cannot be explained by PDK-mediated inhibition of PDH (Extended Data Fig. 5b), and the presence of oxygen suggests that oxygen-dependent lipid desaturation also cannot explain inhibition of lipid synthesis and cell proliferation in these experiments. Furthermore, adding a mixture of exogenous lipids to phenformin-treated cells

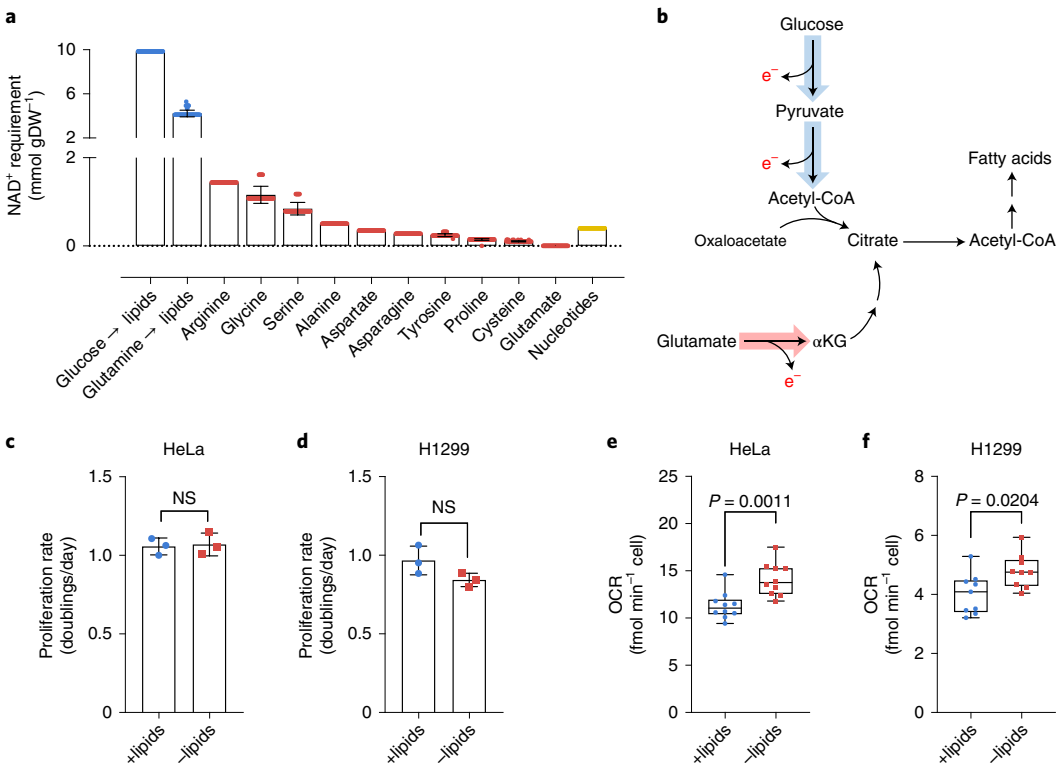

Fig. 1 | Increased lipid synthesis results in increased oxygen consumption and is predicted to increase cellular demand for NAD⁺. **a**, Quantitative predictions for the NAD⁺ consumption cost of de novo synthesis of biomass components lipids (blue), nonessential amino acids (red) and nucleotides (yellow) based on metabolic flux modeling. The NAD⁺ consumption cost is shown separately for synthesis of lipids via oxidative glucose metabolism (glucose → lipids) and reductive glutamine metabolism (glutamine → lipids). Error bars denote the standard deviations of costs calculated across models of NCI-60 cancer cell lines. Each individual value denotes a single cell line prediction from the NCI-60 panel ($n = 60$ independent cell lines from NCI-60). **b**, Schematic showing routes of citrate production and their associated requirements for electron (e^-) disposal. Reactions requiring e^- disposal either directly or indirectly require NAD⁺ as an e^- acceptor. **c**, Cell culture medium was prepared with delipidated serum, and then reconstituted with 1% lipid mixture (2 μg ml⁻¹ arachidonic acid and 10 μg ml⁻¹ each of linoleic, linolenic, myristic, oleic, palmitic and stearic acids, and 0.22 mg ml⁻¹ cholesterol) (+lipids) or vehicle (−lipids). Proliferation rate of HeLa cells cultured in media +lipids or −lipids as indicated ($n = 3$ per condition from a representative experiment). **d**, Proliferation rate of H1299 cells cultured in media +lipids or −lipids as indicated ($n = 3$ per condition from a representative experiment). NS, not significant. **e**, Mitochondrial OCR of HeLa cells cultured in media +lipids or −lipids as indicated. **f**, Mitochondrial OCR of H1299 cells cultured in media +lipids or −lipids as indicated. In **e** and **f**, data are represented as box-and-whisker plots displaying the median, interquartile range (boxes) and minima and maxima (whiskers; $n = 10$ per condition from a representative experiment). In **c** and **d**, bar graphs show means with error bars representing ± s.d. Depicted P values were calculated using unpaired Student's t-test. All experiments were repeated three or more times.

rescued proliferation to the rates observed in culture conditions with non-delipidated serum (Extended Data Fig. 2d). The addition of individual lipids such as oleate and/or mevalonate was partially able to recapitulate the effects of adding the lipid mixture, suggesting that ETC inhibition is limiting lipid synthesis en masse, rather than through production of any individual lipid species (Extended Data Fig. 2e,f). Taken together, these data suggest that the deficit in NAD⁺ regeneration substantially contributes to downregulation of lipid synthesis and reduces cancer cell proliferation in the absence of exogenous lipids.

To further test whether de novo lipogenesis is limited by NAD⁺ regeneration in hypoxia or when electron transport is inhibited, we investigated whether providing an alternative electron acceptor such as pyruvate would rescue cell proliferation in delipidated media, as exogenous pyruvate can be converted to lactate to regenerate NAD⁺[56,57]. Indeed, we found that addition of pyruvate increased the NAD⁺/NADH ratio and the proliferation rate of cells exposed to mitochondrial electron transport inhibitors (Fig. 2b–d and Extended Data Fig. 3a–c) as well as cells in hypoxia (Fig. 2a and Extended Data Fig. 2a). Pyruvate addition also increased intracellular citrate levels (Fig. 2e) and the rate of palmitate synthesis (Fig. 2f). Because synthesis of lipids from citrate-derived acetyl-CoA also requires ATP hydrolysis for the ATP citrate lyase and acetyl-CoA carboxylase (ACC) reactions[58], we considered the possibility that pyruvate is fueling ATP generation through the TCA cycle to rescue proliferation[39]. To test this, we assessed the ability of lactate to rescue fatty acid synthesis and cell proliferation in the same conditions. Similarly to pyruvate, lactate can be metabolized by cells[59,60] to provide carbons for citrate and ATP production, but lactate shifts the equilibrium of the lactate dehydrogenase (LDH) reaction toward pyruvate formation and NAD⁺ consumption[10,56,57,61]. While lactate increased intracellular levels of pyruvate (Fig. 2g), it did not increase the NAD⁺/NADH ratio, intracellular levels of citrate, palmitate synthesis or cell proliferation (Fig. 2a–f and Extended Data Figs. 2a and 3a–c). These results suggest that lipid synthesis is not limited by ATP generation or carbon availability when mitochondrial electron transport is impaired, but rather by the oxidative transformations that are required to produce lipogenic citrate. Notably, neither pyruvate nor lactate had any effect on phenformin-induced ACC phosphorylation (Extended Data Fig. 5a), a marker of increased AMP-activated protein kinase activity that is upregulated in cells experiencing

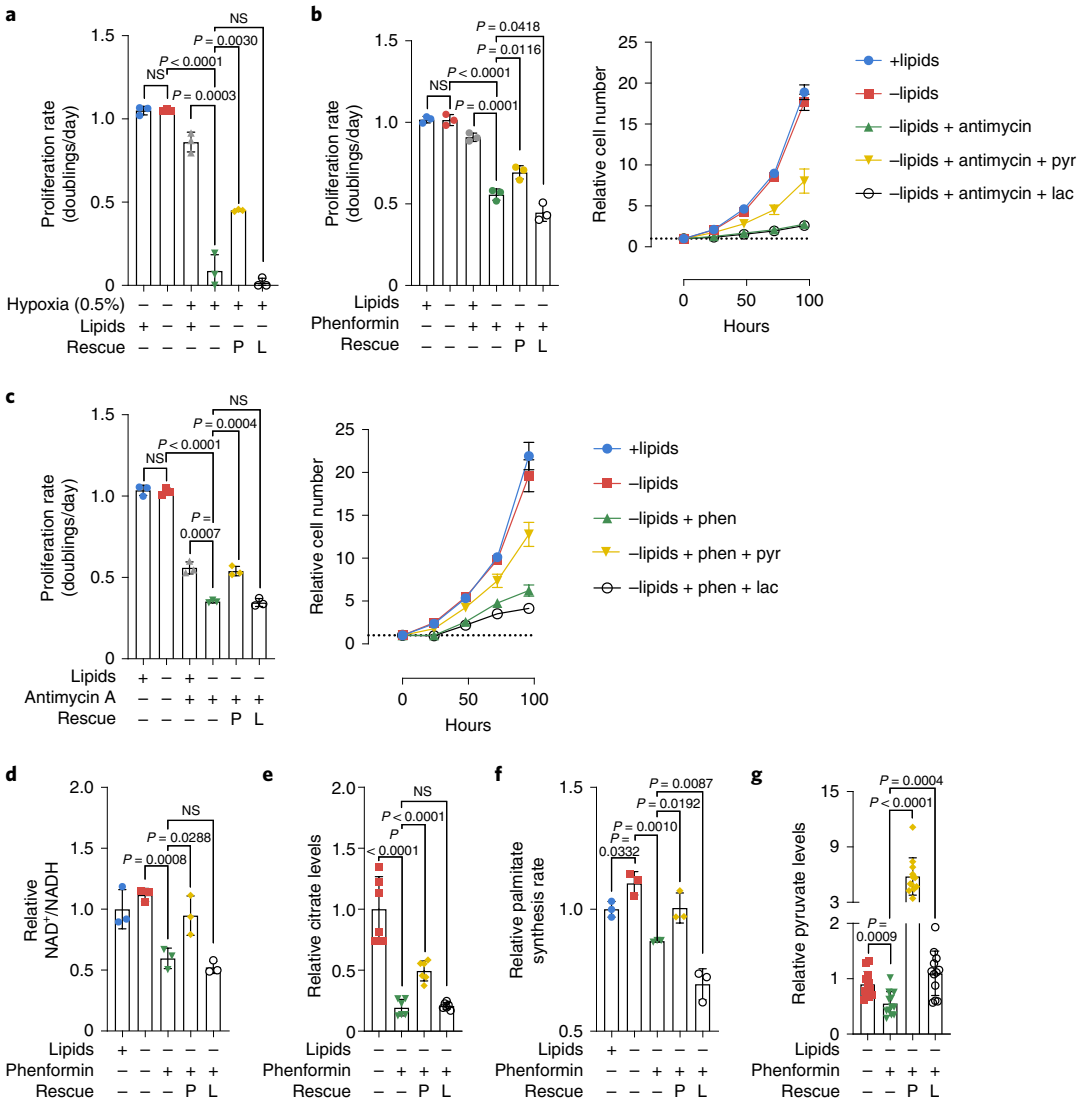

Fig. 2 | Electron acceptor availability dictates proliferation rate in the absence of exogenous lipids. a, Proliferation rates of HeLa cells cultured in media +lipids or −lipids in normoxia (21% oxygen) or hypoxia (0.5% oxygen), without or with pyruvate (1 mM, P) and/or lactate (10 mM, L) as indicated ($n = 3$ per condition from a representative experiment). **b**, Bar chart shows the proliferation rates of HeLa cells cultured in media +lipids or −lipids, without or with phenformin (100 μM), pyruvate (1 mM, P), and/or lactate (10 mM, L) as indicated. Line graph shows the cell number over time of HeLa cells cultured in media +lipids or −lipids, without or with phenformin (100 μM), pyruvate (1 mM, P) and/or lactate (10 mM, L) as indicated ($n = 3$ per condition from a representative experiment). **c**, Bar chart shows the proliferation rates of HeLa cells cultured in media +lipids or −lipids, without or with antimycin A (200 nM), pyruvate (1 mM, P) and/or lactate (10 mM, L) as indicated. Line graph shows cell number over time of HeLa cells cultured in media +lipids or −lipids, without or with antimycin A (200 nM), pyruvate (1 mM, P) and/or lactate (10 mM, L) as indicated ($n = 3$ per condition from a representative experiment). **d**, Relative NAD^+/NADH ratio in HeLa cells cultured in media +lipids or −lipids, without or with phenformin (100 μM), pyruvate (1 mM, P) and/or lactate (10 mM, L) as indicated ($n = 3$ per condition from a representative experiment). **e**, Relative intracellular citrate levels in HeLa cells cultured in media +lipids or −lipids, without or with phenformin (100 μM), pyruvate (1 mM, P) and/or lactate (10 mM, L) as indicated ($n = 3$ per condition from a representative experiment). **f**, Relative palmitate synthesis rates of HeLa cells cultured in media +lipids or −lipids, without or with phenformin (100 μM), pyruvate (1 mM, P) and/or lactate (10 mM, L) as indicated ($n = 3$ per condition from a representative experiment). **g**, Relative intracellular pyruvate levels in HeLa cells cultured in media +lipids or −lipids, without or with phenformin (100 μM), pyruvate (1 mM, P) and/or lactate (10 mM, L) as indicated ($n = 3$ per condition from a representative experiment). All bar charts and line graphs show means with error bars representing ± s.d. Depicted *P* values were calculated using unpaired Student's *t*-tests. All experiments were repeated three or more times.

energy stress[62], potentially explaining why proliferation is only partially rescued in pyruvate-treated cells. We also found that orthogonal methods of increasing the NAD^+/NADH ratio, such as supplementation with α-ketobutyrate, an alternative electron acceptor[11,20], or expression of the *Lactobacillus brevis* NADH oxidase enzyme (*lb*NOX), which regenerates NAD^+ by direct transfer of electrons to oxygen[16], rescued proliferation of phenformin-treated cells cultured in the absence of exogenous lipids (Extended Data Fig. 3g,h). The addition of lipids to phenformin-treated cells did not rescue the proliferation rate beyond the rate observed with pyruvate or α-ketobutyrate rescues alone, consistent with the notion that lipids and alternative electron acceptors rescue proliferation through similar mechanisms (Extended Data Fig. 3d–f). The supplementation of aspartate, previously shown to rescue some

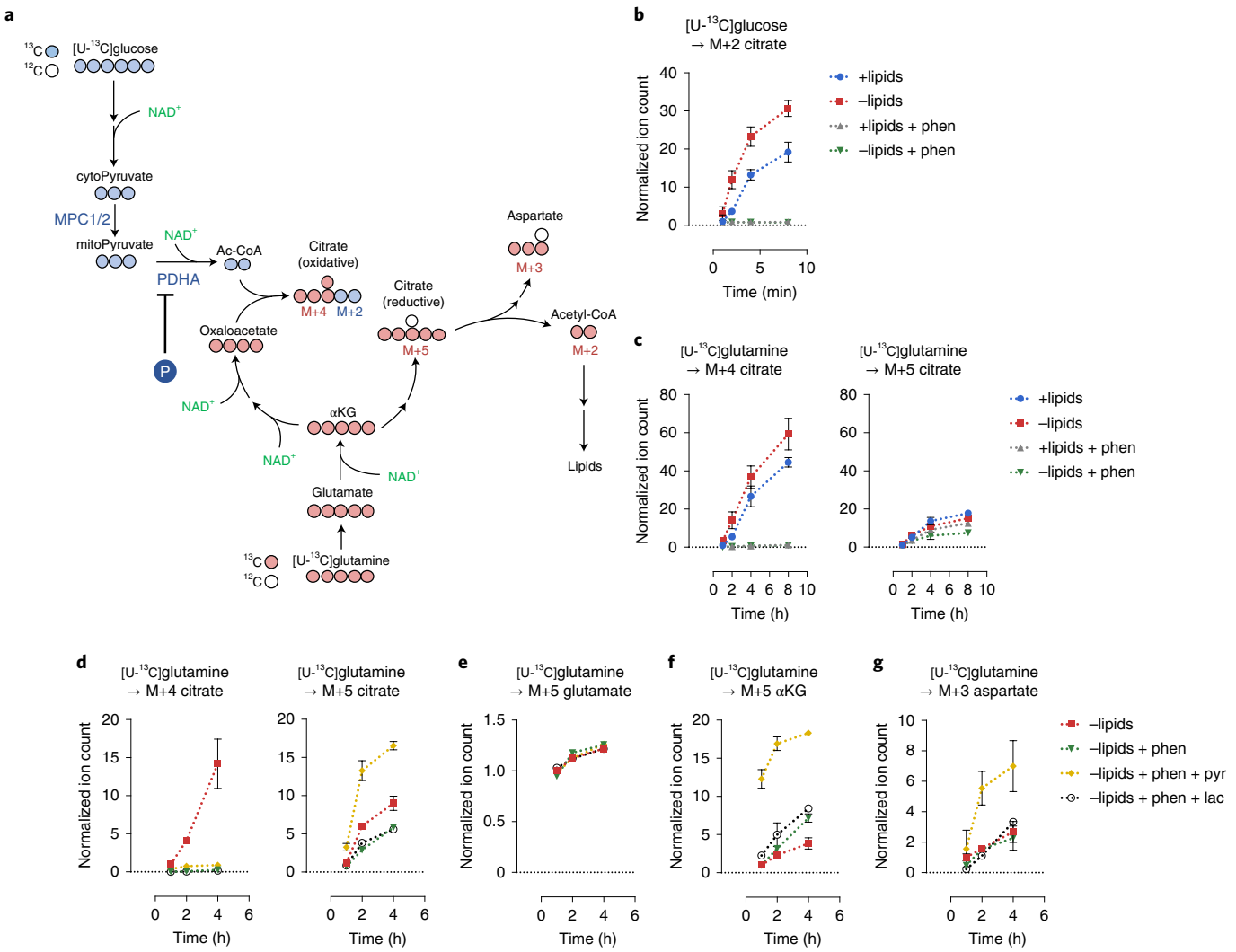

Fig. 3 | Electron acceptor limitation suppresses oxidative and reductive citrate production. a, Schematic depicting carbon transitions involved in the oxidative and reductive pathways to generate citrate from glucose and glutamine. Oxidation of glucose carbons requires mitochondrial pyruvate entry, mediated through MPC1/2, as well as PDHA activity, which is negatively regulated by PDHA phosphorylation (P). Oxidatively produced citrate will be labeled on two carbons (M + 2) from [U-^{13}C]glucose or four carbons (M + 4) from [U-^{13}C]glutamine. Reductively produced citrate will be labeled on five carbons (M + 5) from [U-^{13}C]glutamine; cleavage of M + 5 citrate will yield three-carbon-labeled oxaloacetate (M + 3), which is in equilibrium with M + 3 aspartate. **b**, Assessment of oxidative metabolism via production of M + 2 citrate from [U-^{13}C]glucose over time in HeLa cells cultured in media +lipids or −lipids, with and without phenformin (100 μM, phen) as indicated. Data were normalized to M + 2 citrate in +lipids at $t = 2$ min. **c**, Assessment of oxidative and reductive glutamine metabolism to produce M + 4 and M + 5 citrate from [U-^{13}C]glutamine over time in HeLa cells cultured in media +lipids or −lipids, with and without phenformin (100 μM). **d**, Assessment of M + 4 and M + 5 citrate production from [U-^{13}C]glutamine over time in HeLa cells cultured in medium −lipids, without or with phenformin (100 μM), without or with pyruvate (1 mM, pyr) or lactate (10 mM, lac). In **c** and **e**, data were normalized to M + 4 citrate in +lipids at $t = 1$ h. **e**, Assessment of M + 5 glutamate production over time from [U-^{13}C]glutamine in HeLa cells cultured in medium −lipids without or with phenformin (100 μM), without or with pyruvate (1 mM, pyr) or lactate (10 mM, lac). **f**, Assessment of M + 5 αKG production over time from [U-^{13}C]glutamine in HeLa cells cultured in medium −lipids without or with phenformin (100 μM), without or with pyruvate (1 mM, pyr) or lactate (10 mM, lac). **g**, Assessment of M + 3 aspartate production over time from [U-^{13}C]glutamine in HeLa cells cultured in medium −lipids without or with phenformin (100 μM), without or with pyruvate (1 mM, pyr) or lactate (10 mM, lac). In **e**–**g**, data were normalized to the measured labeled metabolite in −lipids at $t = 1$ h. In **b**–**g**, $n = 3$ biological replicates were examined. Line graphs show means with error bars representing ±s.d. All experiments were repeated three times or more.

conditions of electron acceptor limitation[11,13], was unable to rescue proliferation of cells treated with phenformin and cultured in the absence of exogenous lipids (Extended Data Fig. 4a–c). This result suggests, in agreement with a quantitative prediction of our model (Fig. 1a), that in lipid-depleted conditions the oxidative demand of lipid production can substantially exceed that of aspartate production. More generally, our results argue that beyond the availability of molecular oxygen for desaturation reactions[25], mitochondrial respiration or alternative pathways for NAD$^+$ regeneration are required for biosynthesis of fatty acids.

Both oxidative and reductive tricarboxylic acid cycle lipogenic fluxes are gated by NAD$^+$ availability. To better understand the specific metabolic pathways and reactions that support de novo fatty acid synthesis, we next performed kinetic isotope tracing experiments to assess the metabolic fates of [U-^{13}C]glucose or

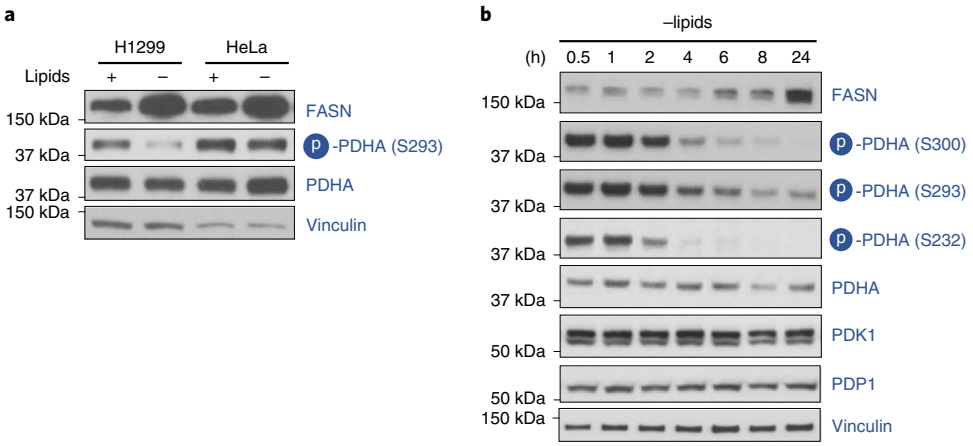

Fig. 4 | Lipid starvation induces dephosphorylation of PDHA. a, Immunoblot analysis of FASN expression, PHDA Ser293 phosphorylation and total PDHA expression. Vinculin was used as a loading control. **b**, Representative immunoblot of FASN, phosphorylated PDHA (Ser232, Ser293 and Ser300), total PDHA, PDK1, PDP1 and vinculin in HeLa cells starved of lipids over time. All experiments were repeated three times or more.

[U-^{13}C]glutamine. We found that culturing cells in the absence of exogenous lipids increased citrate synthesis from both glucose and glutamine via oxidative TCA cycling as measured by the rate of two-carbon-labeled citrate (M+2) formation from [U-^{13}C]glucose, or the rate of four-carbon-labeled citrate (M+4) formation from [U-^{13}C]glutamine (Fig. 3a–c). These data indicate that cancer cells use oxidative pathways with high NAD$^+$ requirements for fatty acid synthesis from glucose when electron acceptors are available. In agreement with isotopic-labeling experiments, the increased oxidative metabolism in lipid starvation conditions was accompanied by an increase of FASN expression and a decrease of the inhibitory Ser293 phosphorylation on the PDH E1/A subunit (Fig. 4a). Further investigation into the kinetics of PDH phosphorylation revealed that the three sites of inhibitory phosphorylation—Ser232, Ser293 and Ser300—were dephosphorylated in HeLa cells as rapidly as 2 h after lipid starvation (Fig. 4b). Notably, we were unable to detect any changes in expression of PDK1 or PDH phosphatase 1 (PDP1) even after 24 h of lipid depletion. Relative to the kinetics of PDH phosphorylation, upregulation of FASN, which is a target of the sterol response element binding protein (SREBP), was much slower, with a detectable increase in expression occurring at ~6 h after lipid starvation (Fig. 4b)[63]. To directly test if the observed changes in PDH phosphorylation can be attributed to known transcriptional responses to lipid starvation, we overexpressed constitutively mature cleaved SREBP1a (mSREBP1a) in HeLa and H1299 cells[64]. While mSREBP1a was able to induce expression of FASN in both HeLa and H1299 cells, it was unable to elicit any changes in PDH Ser293 phosphorylation or in total PDH levels (Extended Data Fig. 5b). These data suggest that a cellular response to lipid starvation in normoxia is initiated by a fast posttranscriptional rewiring of central carbon metabolism to favor oxidative citrate production, followed by a slower transcriptional upregulation of enzymes responsible for fatty acid biosynthesis.

Previous work has shown that hypoxia or pharmacological inhibition of mitochondrial electron transport result in a decreased fractional contribution of glucose carbon to lipogenic citrate, and a concomitant increase in the fractional contribution of glutamine carbon via reductive carboxylation of glutamine-derived αKG[31–33]. In agreement with these findings, culturing cells with phenformin in the presence or absence of exogenous lipids decreased M+4 citrate labeling and increased M+5 citrate labeling from [U-^{13}C] glutamine (Extended Data Fig. 6a). These changes were also accompanied by an increase in the αKG/citrate ratio (Extended Data Fig. 6b), also consistent with previous observations[46,54]. The change in αKG/citrate ratio was largely driven by a decrease in total citrate levels (Extended Data Fig. 6c). Surprisingly, kinetic tracing measurements in phenformin-treated cells revealed that the rates of both oxidative and reductive glutamine fluxes substantially decreased compared to untreated cells (Fig. 3c). The flux measurements, alongside smaller citrate levels under conditions of ETC inhibition, suggest that reductive carboxylation cannot fully compensate for decreased citrate synthesis from glucose when NAD$^+$ is limited. Thus, these results support the computational prediction that both oxidative and reductive pathways of lipogenic citrate synthesis incur NAD$^+$ consumption costs, and that both routes are compromised when the NAD$^+$/NADH ratio decreases (Fig. 1a).

Using tracing experiments, we next sought to determine how the addition of pyruvate can increase intracellular citrate levels and upregulate fatty acid synthesis. To that end, we traced [U-^{13}C] glutamine to assess the rate of oxidative M+4 and reductive M+5 citrate formation (Fig. 3a). In cells cultured with delipidated media and phenformin, the addition of pyruvate, but not lactate, increased the rates of citrate production through both oxidative and reductive routes; however, the rate of glutamine reductive carboxylation far exceeded the rates of glucose and glutamine oxidation (Fig. 3d). The elevated rate of reductive carboxylation appears to be facilitated by increased αKG production from glutamate and not by increased glutamate production from glutamine (Fig. 3e,f). As the conversion of glutamate to αKG transforms a carbon–nitrogen bond into a carbon–oxygen double bond, the reaction is overall oxidative, and therefore likely depends on the NAD$^+$/NADH ratio irrespective of whether this conversion proceeds through glutamate dehydrogenase or any transamination reaction[11,42]. We also confirmed that the citrate produced via reductive glutamine flux was further metabolized by ATP citrate lyase to generate lipogenic acetyl-CoA, as the rate of M+3 aspartate production from [U-^{13}C]glutamine was specifically elevated in the pyruvate-treated, but not in the lactate-treated cells (Fig. 3g).

To further corroborate the finding that pyruvate facilitates citrate production through its effects on NAD$^+$ regeneration, and not due to pyruvate serving as a carbon source, we repeated the kinetic [U-^{13}C]glutamine tracing experiments with the alternative electron acceptor α-ketobutyrate. As with pyruvate, α-ketobutyrate facilitated reductive citrate production from glutamine, and upregulation in the reductive TCA cycle flux similarly originated from an increased rate of conversion of glutamate to αKG (Fig. 5a–d). Thus, when mitochondrial electron transport is impaired, providing

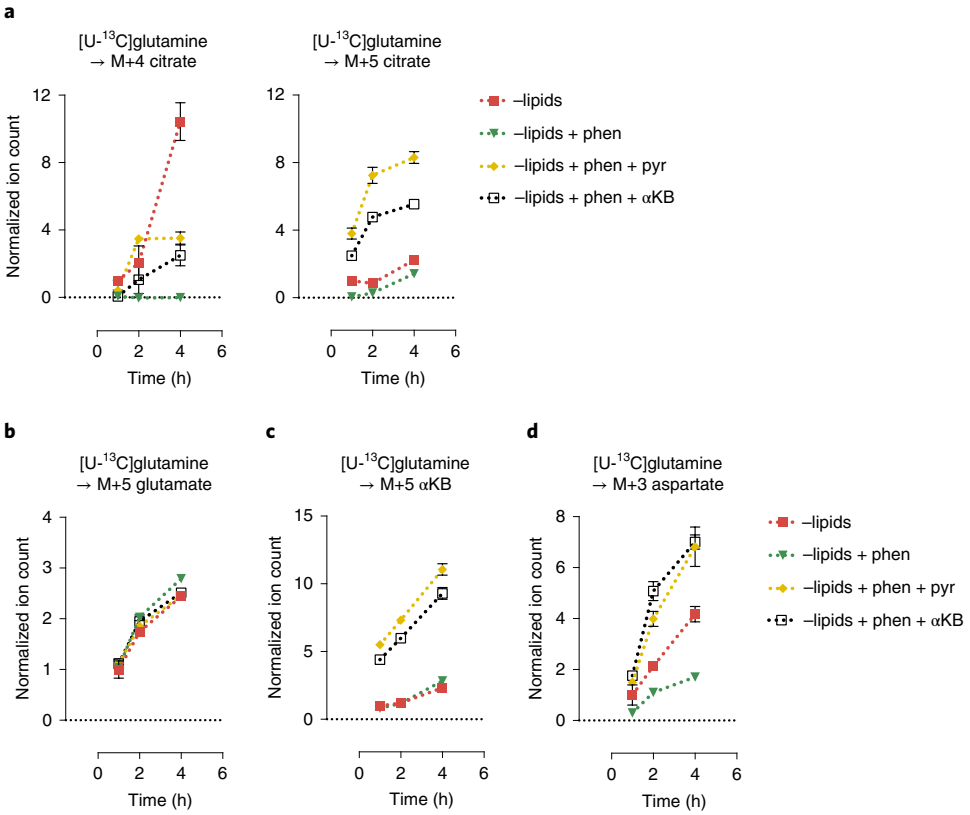

Fig. 5 | Reductive tricarboxylic acid cycle flux is gated by electron acceptor availability. a, Assessment of M+4 and M+5 citrate production from [U-^{13}C]glutamine over time in HeLa cells cultured in medium −lipids, without or with phenformin (100 μM), without or with pyruvate (1 mM, pyr) or alpha-ketobutyrate (1 mM, αKB) as indicated. **b**, Assessment of M+5 glutamate production over time from [U-^{13}C]glutamine in HeLa cells cultured in medium −lipids without or with phenformin (100 μM), without or with pyruvate (1 mM) or αKB (1 mM) as indicated. **c**, Assessment of M+5 αKG production over time from [U-^{13}C]glutamine in HeLa cells cultured in medium −lipids without or with phenformin (100 μM), without or with pyruvate (1 mM) or αKB (1 mM) as indicated. **d**, Assessment of M+3 aspartate production over time from [U-^{13}C]glutamine in HeLa cells cultured in medium −lipids without or with phenformin (100 μM), without or with pyruvate (1 mM) or αKB (1 mM) as indicated. Data were normalized to M+4 citrate in **a** and to the corresponding labeled metabolite in **b**–**d** in −lipids at $t=1$ h.

alternative electron acceptors rescues lipogenic citrate synthesis primarily through reductive glutamine carboxylation.

Because mitochondrial respiration and LDH regenerate NAD$^+$ in different cellular compartments, we next wondered if the mechanism of stimulating reductive citrate production when electron transport is inhibited depends on the location of NAD$^+$ regeneration. To address this question, we expressed *lb*NOX in the cytosol or mitochondria of HeLa cells[16] and then performed kinetic [U-^{13}C]glutamine tracing in lipid-depleted conditions (Fig. 6a). We observed that both cytosolic and mitochondrial *lb*NOX increased basal oxidative and reductive citrate production (Fig. 6b,c). In the presence of phenformin, oxidative and reductive citrate production were inhibited, and cells expressing *lb*NOX and mito-*lb*NOX produced the majority of citrate via reductive glutamine metabolism. Similarly to exogenous electron acceptors, the expression of either *lb*NOX or mito-*lb*NOX predominantly increased the conversion of glutamate to αKG (Fig. 6d–f). Taken together, these experiments support the observation that both oxidative and reductive carboxylation routes of fatty acid synthesis can be inhibited at oxidative reaction steps in hypoxia or when electron acceptors are limited. However, when cells are provided with alternative methods of generating electron acceptors in the context of mitochondrial electron transport inhibition, reductive carboxylation becomes the preferred route of producing lipogenic citrate.

Acetate bypasses NAD$^+$-consuming reactions and reduces dependence on environmental lipids. Exogenous acetate can be metabolized by cancer cells in culture and by tumors[65,66]. Previous studies have shown that acetate can have various and context-dependent metabolic fates, from participating in epigenetic modifications to serving as a carbon source for lipid synthesis, with higher usage of acetate for lipid synthesis in hypoxia[65,67–69]. We rationalized that our findings provide a novel mechanistic explanation for the ability of acetate to support cell proliferation in electron acceptor-limited conditions[70]. Specifically, acetate could circumvent the NAD$^+$-consuming reactions that are essential for synthesis of cytosolic acetyl-CoA. Indeed, exogenous acetate rescued proliferation of cells cultured in lipid-depleted conditions in the presence of phenformin or antimycin A (Fig. 7a,b and Extended Data Fig. 7a,b) without altering the intracellular NAD$^+$/NADH ratio (Fig. 7c and Extended Data Fig. 7c). Acetate also restored proliferation of lipid-deprived cells in hypoxia (Fig. 7g and Extended Data Fig. 7d). Consistent with its role as a carbon source for fatty acid synthesis, exogenous acetate also increased palmitate synthesis rate (Fig. 7d) without changing citrate levels (Fig. 7e), TCA cycle fluxes (Fig. 7f), levels of TCA cycle metabolic intermediates (Extended Data Fig. 8a–d) or ACC phosphorylation (Extended Data Fig. 5a). These data argue that acetate restores fatty acid synthesis by circumventing the NAD$^+$ requirement for citrate production. Notably, acetate rescues lipid biosynthesis despite being incorporated into lipogenic

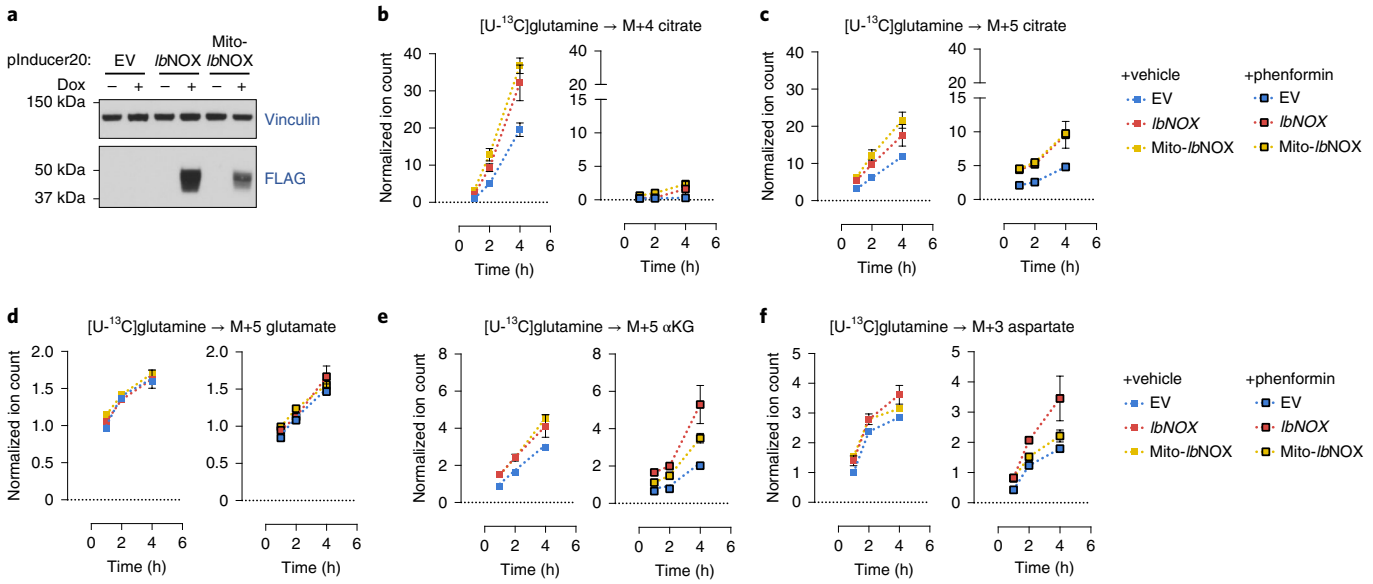

Fig. 6 | Complementation of electron transport chain with NADH oxidase stimulates reductive tricarboxylic acid cycle flux. a, Immunoblot of HeLa cells expressing empty vector (EV), FLAG-tagged *Lactobacillus brevis* NADH oxidase (*lb*NOX), or mitochondrial localized FLAG-tagged *Lactobacillus brevis* NADH oxidase (Mito-*lb*NOX) under a doxycyline-inducible promoter treated with or without 0.5 μg ml^{-1} doxycycline (dox). **b**, Assessment of M+4 citrate production from [U-^{13}C]glutamine over time in HeLa cells expressing EV, *lb*NOX or mito-*lb*NOX cultured in medium −lipids, with 0.5 μg ml^{-1} doxycycline, without or with phenformin (100 μM) as indicated. **c**, Assessment of M+5 citrate production from [U-^{13}C]glutamine over time in HeLa cells expressing EV, *lb*NOX or mito-*lb*NOX cultured in medium −lipids, with 0.5 μg ml^{-1} doxycycline, without or with phenformin (100 μM) as indicated. **d**, Assessment of M+5 glutamate production over time from [U-^{13}C]glutamine in HeLa cells expressing EV, *lb*NOX or mito-*lb*NOX cultured in medium −lipids, with 0.5 μg ml^{-1} doxycycline, without or with phenformin (100 μM) as indicated. **e**, Assessment of M+5 αKG production over time from [U-^{13}C]glutamine in HeLa cells expressing EV, *lb*NOX or mito-*lb*NOX cultured in medium −lipids, with 0.5 μg ml^{-1} doxycycline, without or with phenformin (100 μM) as indicated. **f**, Assessment of M+3 aspartate production over time from [U-^{13}C]glutamine in HeLa cells expressing EV, *lb*NOX or mito-*lb*NOX cultured in medium −lipids, with 0.5 μg ml^{-1} doxycycline, without or with phenformin (100 μM) as indicated. Data were normalized to M+4 citrate in **b** and to the corresponding labeled metabolite in **c**–**f** in HeLa EV cells at $t=1$ h. In **b**–**f**, $n=3$ biological replicates were examined. All line graphs show means with error bars representing ±s.d. All experiments were repeated three times or more.

acetyl-CoA multiple reactions upstream of the lipid desaturation reactions that consume molecular oxygen. This further supports the crucial role played by NAD$^+$-consuming reactions in gating lipid synthesis in hypoxia. The conversion of exogenous acetate to lipogenic acetyl-CoA also consumes ATP[71], in agreement with a model in which lipid biosynthesis is primarily limited by the NAD$^+$/NADH ratio rather than ATP availability in electron acceptor-depleted conditions.

Gene expression analysis suggests that de novo lipid biosynthesis is downregulated in hypoxia across tumors. To explore whether de novo lipid synthesis in tumors is affected by conditions where electron acceptors are limited in vivo, we next investigated if hypoxia was associated with coordinated changes in metabolic gene expression across human tumors. We used RNA-sequencing data from The Cancer Genome Atlas (TCGA) to calculate the correlations between mRNA expression of the 87 metabolic pathways defined in the Kyoto Encyclopedia of Genes and Genomes (KEGG)[72] and expression of known tumor hypoxia markers[30,73]. Interestingly, analysis of over 10,000 primary tumor samples demonstrated that among all considered metabolic pathways, lipid biosynthesis has one of the strongest negative correlations with the expression signature of tumor hypoxia (Pearson's $R=-0.39$, $P<10^{-16}$, Bonferroni corrected; Fig. 8a,b). The correlation was also significant when controlling for the potential effects of tumor proliferation rate, using purine, pyrimidine or transfer RNA synthesis as a proxy for proliferation rate (partial Pearson's correlation $R=-0.39$, $P<10^{-16}$, $R=-0.38$, $P<10^{-16}$ and $R=-0.32$, $P<10^{-16}$, respectively). Of the 34 investigated tumor types, 29 individually displayed a significant negative correlation (at 1% false discovery rate) between hypoxia and fatty acid biosynthesis (Extended Data Fig. 9a,b), confirming that this effect is observed generally across tumors. We next investigated the regulatory mechanisms that may mediate the transcriptional response of lipid biosynthesis genes to hypoxia. While it is unlikely that a universal regulatory mechanism mediates this response in all tumors, we found that the expression of *SREBF1* and *SREBF2*—whose products, SREBP1/2, are canonical regulators of lipid biosynthesis—is strongly correlated with the expression of fatty acid biosynthesis genes across the entire expression range of hypoxia markers (Extended Data Fig. 10a)[74]. We also observed that SREBP2 expression is significantly anti-correlated with hypoxia markers (Pearson $r=-0.22$, $P<1\times10^{-16}$). These results suggest that SREBPs are likely to be involved in regulating lipid synthesis both in normoxia and hypoxia, but further investigation into various regulatory mechanisms of lipid sensing in hypoxia and expression response in specific tumor types is warranted.

Analysis of the TCGA expression data also demonstrated that across all tumor samples, the hypoxia expression signature positively correlated with the expression of genes involved in fatty acid uptake (Pearson's $R=0.41$, $P<10^{-16}$; Fig. 8c), and this finding was also significant in 28 out of the 34 tumor types analyzed individually (at 1% false discovery rate; Extended Data Fig. 9a,c). Of note, while hypoxia markers strongly correlated with lipid uptake genes and anti-correlated with lipid biosynthesis genes (Fig. 8), the correlation between hypoxia markers and *SCD1*, a gene involved in lipid desaturation, was relatively weak (Extended Data Fig. 10b) both across all tumors (Pearson's $r=0.03$, $P=0.002$), and for individual tumor types (out of 34 TCGA tumor types, 24 did not exhibit a significant

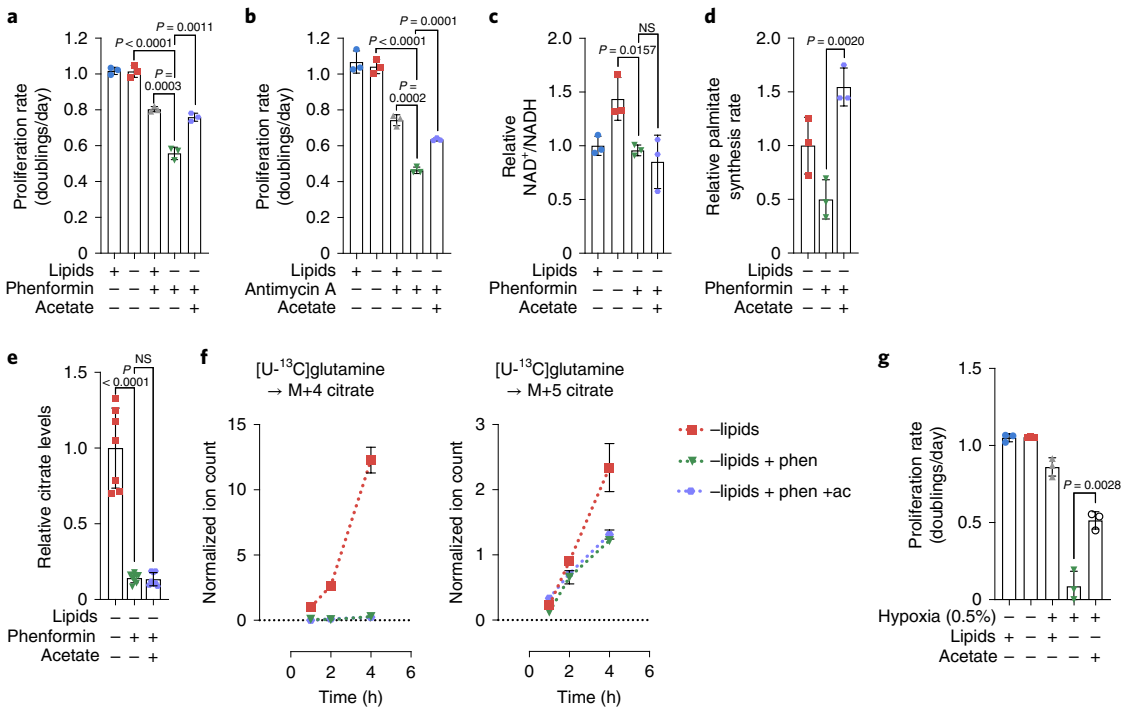

Fig. 7 | Bypassing oxidative steps in fatty acid synthesis rescues proliferation in electron acceptor-deficient cells. a, Proliferation rates of HeLa cells cultured in media +lipids or −lipids, without or with phenformin (100 μM) or acetate (200 μM) as indicated ($n=3$ per condition from a representative experiment). **b**, Proliferation rates of HeLa cells cultured in media +lipids or −lipids, without or with antimycin A (200 nM) or acetate (200 μM) as indicated ($n=3$ per condition from a representative experiment). **c**, Relative NAD^+/NADH ratio in HeLa cells cultured in media +lipids or −lipids, without or with phenformin (100 μM) or acetate (200 μM) as indicated ($n=3$ per condition from a representative experiment). **d**, Relative palmitate synthesis rates of HeLa cells cultured in medium −lipids without or with phenformin (100 μM) or acetate (200 μM) as indicated ($n=3$ per condition from a representative experiment). **e**, Relative intracellular citrate levels in HeLa cells cultured in medium −lipids without or with phenformin (100 μM) or acetate (200 μM) as indicated ($n=3$ per condition from a representative experiment). **f**, Assessment of M+4 and M+5 citrate production from [U-^{13}C]glutamine over time in HeLa cells cultured in medium −lipids without or with phenformin (100 μM) or acetate (200 μM) as indicated. Data were normalized to M+4 citrate in −lipids at $t=1$ h ($n=3$ per condition from a representative experiment). **g**, Proliferation rates of HeLa cells cultured in media +lipids or −lipids, in normoxia (21% oxygen) or hypoxia (0.5% oxygen), and without or with acetate (200 μM) as indicated. Data from the first four conditions are the same as those presented in Fig. 2a. ($n=3$ per condition). Depicted P values were calculated using unpaired Student's t-tests. All experiments were repeated three times or more.

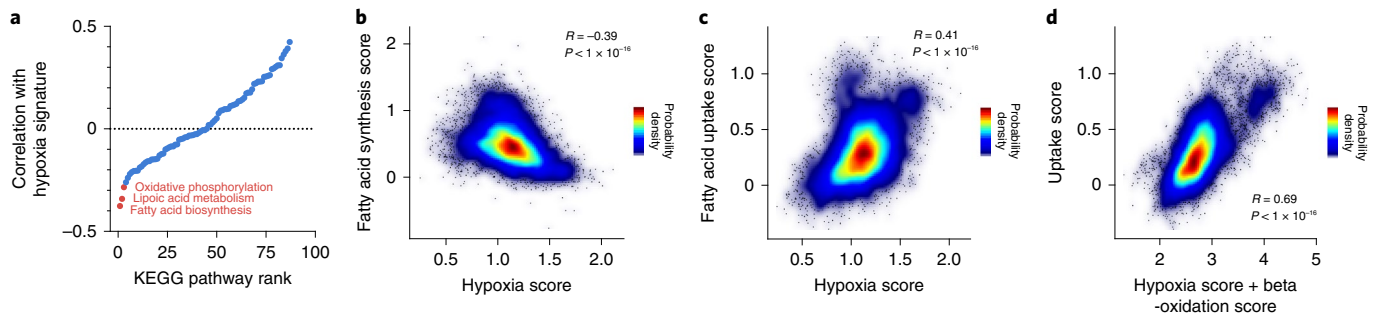

Fig. 8 | Correlations between mRNA expression of fatty acid synthesis or fatty acid uptake genes and markers of tumor hypoxia. a, Ranking of 87 KEGG metabolic pathways based on the correlation between expression of their genes with expression of known markers of tumor hypoxia (tumor hypoxia scores); the correlations were calculated using TCGA expression data, such that stronger negative correlations correspond to stronger anti-correlations with hypoxia markers. **b**, Correlation between the tumor hypoxia score and expression of genes involved in fatty acid synthesis. **c**, Correlation between the tumor hypoxia score and expression of genes participating in fatty acid uptake. **d**, Correlation between the mRNA expression of gene markers of lipid uptake and the sum of mRNA expression of gene markers of hypoxia and beta-oxidation scores. In **b**–**d**, the density plots show relative counts of individual TCGA samples. The Pearson's P values for the correlation coefficients were calculated using two-sided Student's t-tests, with Bonferroni correction where multiple hypotheses were tested.

correlation). These results are consistent with our biochemical analysis indicating that lipid desaturation is unlikely to be the primary or the only bottleneck for lipid synthesis in hypoxia. Taken together, this analysis suggests that multiple tumor types adapt to hypoxia by downregulating fatty acid synthesis genes and upregulating genes involved in lipid acquisition from the environment. This conclusion

is consistent with previous work showing that hypoxia can alter lipid metabolism in vitro and in vivo[25,26,68], and in agreement with our biochemical analysis demonstrating that lipid synthesis is strongly inhibited in hypoxia.

We next investigated the cellular processes that may explain the considerable variability of lipid uptake across tumors. We rationalized that in addition to growth-related uptake mediated by inhibition of de novo lipid synthesis in hypoxia, a substantial fraction of lipid uptake variability may be also mediated by beta-oxidation, a process important for energy generation in some cancers with low or even intermediate hypoxia[44]. Interestingly, we found that a simple linear combination of the expression of beta-oxidation gene markers and hypoxia gene markers can indeed explain about half of the variance in the expression of lipid uptake markers across all tumors (Fig. 8d; Pearson $r=0.69$, $P<10^{16}$). This result suggests that the adaptation of lipid synthesis to hypoxia and the utilization of lipids for beta-oxidation are the two major cellular processes explaining the diversity of lipid uptake across tumors.

Discussion

Cancer cells adapt their metabolism to support proliferation in diverse tissue and environmental contexts[5,6,9,75–77]. Environmental metabolic constraints on cancer cell proliferation include the availability of nutrients, such as exogenous amino acids, nucleotides and lipids, as well as access to oxygen. An important metabolic role of environmental oxygen is to serve as a terminal electron acceptor for the regeneration of NAD^+ via mitochondrial respiration to support cellular oxidation reactions. Some tumors, in contrast to many normal tissues, synthesize a substantial fraction of their lipids de novo[44], and lipid synthesis can be essential for tumor growth in tissues where access to environmental lipids is limited[78,79]. Our computational and experimental analyses demonstrate that de novo lipid synthesis incurs a substantial NAD^+ consumption cost, which may dominate the consumption costs of producing other biomass components. Notably, despite lipid biosynthesis being canonically considered to be a reductive process, our results demonstrate that up to 30% of the total oxygen uptake in cells growing without access to environmental lipids is likely due to de novo biosynthesis of lipids. This can make lipogenic citrate production limiting for proliferation in hypoxia or other conditions where NAD^+ regeneration is impaired. This limitation may substantially contribute to the dependence of hypoxic tumors on exogenous acetate and lipids[25,26,68]. We note that a large amount of molecular oxygen is also consumed in reactions involved in the desaturation and maturation of sterols that comprise a substantial fraction of membrane lipids[80]. However, similarly to fatty acid desaturation, oxygen consumption in sterol maturation reactions cannot explain the NAD^+ regeneration bottlenecks located multiple biochemical steps upstream of these reactions.

Previous work has shown that cancer cells can rewire their metabolism to rely on reductive glutamine carboxylation for lipid synthesis when mitochondrial respiration is impaired[31–33]. Because the usage of glutamine carbon to synthesize fatty acids is chemically net reductive, it might be expected that this pathway is upregulated in hypoxia or in the presence of mitochondrial electron transport inhibitors that compromise NAD^+ regeneration. However, surprisingly, we find that this net reductive pathway is also impaired in the absence of exogenous electron acceptors. Notably, this impairment cannot be explained by known metabolic regulatory mechanisms, such as phosphorylation-mediated inhibition of PDH activity, or the requirement for molecular oxygen in lipid desaturation reactions. Rather, our data suggest that reductive carboxylation is gated by NAD^+ availability for the conversion of glutamate to αKG, potentially explaining why this net reductive pathway cannot fully compensate for oxidative lipid synthesis from glucose when electron acceptors are limited. More generally, our work demonstrates that the availability of oxidizing and reducing equivalents required for specific metabolic reactions may gate a biochemical pathway whether or not the pathway is overall net reductive or net oxidative.

Beyond de novo lipid synthesis, the requirement for NAD^+ regeneration to produce other biomass components has been shown in several contexts. A hypoxia-induced auxotrophy for aspartate has been reported in some tumors[12,14], and select cancers are also sensitive to both serine and nucleotide levels[77,81,82]. Our computational model predicts that, in addition to lipids, there can also be a considerable oxidative cost of arginine, glycine and alanine production, consistent with evidence supporting sensitivity of select cancers to some of these nutrients in vivo[83–85]. Deficiencies in NAD^+ regeneration, which is required to synthesize diverse biomass components, may explain why and how various tumors become dependent on specific synthesis pathways or on uptake of specific nutrients available in their environment.

Methods

Computational analysis of the NAD^+ consumption costs associated with synthesis of biomass components. To estimate the NAD^+ consumption costs associated with synthesis of various biomass components, we used the genome-scale FBA model of human cellular metabolism[35] that contains 3,744 reactions and 2,766 metabolites. To constrain internal and exchange metabolic fluxes, we used the experimentally measured NCI-60 cell line fluxomics data[3]. For each cell line in the NCI-60 panel, we constrained the FBA model based on the nutrient exchange fluxes experimentally measured for that cell line, and then pruned the model to identify essential metabolic reactions that are required to synthesize all key biomass components. The consumption costs were then estimated, for each considered biomass component, by solving a linear optimization problem to find the minimal NAD^+ consumption required for the biosynthesis of that component for a unit of cellular biomass (Supplementary Methods).

Metabolic gene expression analysis of primary tumors. To perform pathway expression analysis of primary tumors, we utilized mRNA-sequencing data from ~11,000 primary tumor samples spanning 34 human tumor types from TCGA. For the metabolic pathway analyses, we used metabolic gene annotations from the KEGG database[72]. Using the TCGA data, we calculated correlations between mRNA expression of genes forming distinct metabolic pathways and gene markers of tumor hypoxia and lipid uptake (Supplementary Methods).

Cell culture experiments. Cell lines were maintained in RPMI (Fisher Scientific, MT10040CV) supplemented with 10% fetal bovine serum (FBS). For all experiments, cells were washed three times in phosphate buffered saline (PBS), and then cultured in 4 ml of RPMI with 10% dialyzed FBS, and supplemented with lactate, pyruvate and acetate as indicated. The reagents used for the cell culture experiments are as follows: sodium pyruvate (Sigma, P2256), sodium L-lactate (Sigma, L7022), sodium acetate (Sigma, S2889), Lipid Mixture 1, Chemically Defined (Sigma, L0288), rotenone (Sigma, R8875), phenformin hydrochloride (Sigma, P7045 FLUKA), antimycin A from *streptomyces* sp. (A8676), GSK2194069 (Tocris, 5303), [U-^{13}C]glucose (Cambridge Isotope Laboratories, CLM-1396), [U-^{13}C]glutamine (Cambridge Isotope Laboratories, CLM-1822), [U-^{13}C]pyruvate (Cambridge Isotope Laboratories, CLM-2440), [U-^{13}C]lactate (Cambridge Isotope Laboratories, CLM-1579) and 99% enriched deuterium oxide (Sigma, 151882). All cells were cultured at 37 °C with 5% CO_2. When indicated, +lipid culture conditions refer to RPMI supplemented with 10% delipidated serum and 1% Lipid Mixture 1. The cell lines A549 (CCL-185), PANC-1 (CRL-1469), H1299 (CRL-5803), 143B (CRL-8303) and HeLa (CRM-CCL-2) were acquired from the American Type Culture Collection. The cell line AL1376 was derived from a pancreatic ductal adenocarcinoma isolated from a KP$^{-/-}$CT [*LSL-Kras*$^{G12D/+}$, *TP53*$^{flox/flox}$, *Pdx-1-Cre*, LSL-tdTomato] mouse on a C57BL6/J background. All cell lines were tested for mycoplasma contamination quarterly and confirmed to be negative before experimentation.

Oxygen consumption. An Agilent Seahorse Bioscience Extracellular Flux Analyzer (XF24) was used to measure OCRs. Cells were plated at 50,000 cells per well in Seahorse Bioscience 24-well plates in 50 µl of RPMI supplemented with 10% dialyzed FBS. An additional 500 µl of medium was added following a 1-h incubation. The following day, cells were washed three times with PBS and incubated in RPMI with the indicated treatment, and OCR measurements were made after 5 h of incubation. After OCR data acquisition, each well of the plate was collected for cell number analysis. Basal OCR was calculated by subtracting the residual OCR following the addition of rotenone and antimycin A from the initial OCR measurements.

Proliferation rates. Cells were plated in replicate six-well plates in 2 ml at an initial seeding density of 20,000 cells. Cells were permitted to settle overnight and cells on

a six-well dish were counted to calculate the starting cell number at the initiation of the experiment. For all remaining plates, cells were washed three times with PBS and 4 ml of treatment medium was added to each well. Three days after the initial treatment, cells were quantified using a sulforhdamine B (SRB) colorimetric assay. All SRB measurements were normalized to a blank. Proliferation rates were calculated using Equation (1):

$$\text{Proliferation rate (doublings/day)} = \frac{\log_2\left(\frac{\text{SRB absorbance day 3}}{\text{SRB absorbance day 0}}\right)}{3\,\text{d}} \quad (1)$$

GC–MS metabolite measurements. For polar metabolites, dried samples were derivatized with 20 µl of methoxamine reagent (Thermo Fisher, TS-45950) and 25 µl of *N-tert*-butyldimethylsilyl-*N*-methyltrifluoroacetamide with 1% *tert*-butyldimethylchlorosilane (Sigma 375934). Following derivatization, samples were analyzed using a DB-35MS column (30 m × 0.25 mm i.d. × 0.25 µm, Agilent J&W Scientific) in an Agilent 7890 gas chromatograph coupled to an Agilent 5975C mass spectrometer (GC–MS). For fatty acids, dried samples were first resuspended in 100 µl toluene (Sigma, 650579) and 200 µl of 2% sulfuric acid in methanol was added. Samples were incubated overnight at 50 °C. The next day, 500 µl 5% NaCl and 500 µl hexane (Sigma, 34859) were added to the sample. The top fraction was collected, followed by a second hexane extraction with 500 µl. The hexane fractions were pooled and dried down under nitrogen gas. The dried samples were resuspended in 50 µl hexane and transferred into glass inserts for GC–MS analysis. Fatty acid methyl ester (FAME) samples were analyzed using a DB-FastFAME GC Column, 30 m × 0.25 mm × 0.25 µm, 7-inch configuration, Agilent J&W Scientific) in an Agilent 7890 gas chromatograph coupled to an Agilent 5975C mass spectrometer. The chromatograph method for fatty acid analysis was as follows: hold at 100 °C for 5 min, followed by a ramp of 8 °C per min to 180 °C, then followed by a ramp of 1 °C per min to 230 °C. Data were analyzed and corrected for natural isotope abundance using in-house algorithms and/or MZmine 2.

Dynamic [U-^{13}C]glutamine tracing experiments. Cells were plated in six-well plates at a seeding density of 150,000 cells per well. Cells were permitted to settle overnight. The following day, cells were washed three times with PBS and cultured in the indicated treatment conditions for 24 h until metabolic steady state was reached. For cells expressing pInducer20-EV, pInducer20-*lb*NOX and pInducer20-mito-*lb*NOX, 500 ng ml^{-1} of doxycycline was added to the medium. Before the initiation of the dynamic isotope tracing, cells were washed once with PBS, and then cultured in 2 ml of medium containing the 2 mM [U-^{13}C]glutamine and the indicated treatment condition. For cells expressing pInducer20-EV, pInducer20-*lb*NOX and pInducer20-mito-*lb*NOX, 500 ng ml^{-1} of doxycycline was also added to all treatment and tracer media. Following the appropriate incubation, wells were washed as quickly as possible with ice-cold blood bank saline and lysed on the dish with 400 µl of ice-cold 80% HPLC-grade methanol (Sigma, 646377) in HPLC-grade water (Sigma, 270733) with 1 µg per 400 µl norvaline (Sigma, N7627) to use as an internal extraction standard.

Dynamic [U-^{13}C]glucose tracing experiments. Cells were plated in six-well plates in at a seeding density of 200,000 cells per well. Cells were permitted to settle overnight. The following day, cells were washed three times with PBS and cultured in the indicated treatment conditions for 24 h until metabolic steady state was reached. Before the initiation of the dynamic isotope tracing, cells were washed once with PBS, and then cultured in 1.5 ml of medium containing 5 mM unlabeled glucose and the indicated treatment condition for 5 h. Then, 30 µl of 1 M [U-^{13}C] glucose was added to each well to reach a final glucose enrichment of 80% and incubated for the indicated times. Following the appropriate incubation, cells were washed as quickly as possible with ice-cold blood bank saline and lysed on the dish with 400 µl of ice-cold 80% HPLC-grade methanol (Sigma, 646377) in HPLC-grade water (Sigma, 270733) with 1 µg per 400 µl norvaline (Sigma, N7627) to use as an internal extraction standard.

Palmitate synthesis rate. Cells were plated in six-well plates at a seeding density of 150,000 cells per well. Cells were permitted to settle overnight. Before the initiation of the experiment, cells were washed three times with PBS, and then cultured for 24 h in the indicated treatment condition. After 24 h, medium with the indicated treatment condition and reconstituted with 99% deuterium oxide was added to each well to achieve a final deuterium oxide enrichment of 45%. After 2 h of culture in tracer medium, wells were washed three times as quickly as possible with ice-cold blood bank saline and lysed on the dish with 700 µl of (4:3) methanol:0.88% KCl in water with 0.25 µg ml^{-1} tridecanoic acid (Sigma, T0502) to use as an internal extraction standard. Samples were scraped, collected into glass vials (Thermo Fisher Scientific, C4010-1) and 800 µl HPLC-grade dichloromethane (Thermo Fisher Scientific, 402152) was added. Samples were vortexed for 10 min at 4 °C and centrifuged at 5,000*g* for 10 min at 4 °C. The bottom fraction was collected into glass vials and dried down under nitrogen gas for subsequent FAME analysis by GC–MS. Palmitate synthesis rates were calculated by integrating the sum of all labeled species and normalized to cell number and time of label treatment.

NAD$^+$/NADH measurements. Cells were seeded at 20,000 cells per well in six-well plates and permitted to adhere overnight. Next, cells were washed three times in PBS and incubated in 4 ml of the indicated treatment media for 5 h. Cells were then rapidly washed three times in 4 °C PBS and extracted in 100 µl of ice-cold lysis buffer (1% dodecyltrimethylammonium bromide in 0.2 N of NaOH diluted at a ratio of 1:1 with PBS), snap frozen in liquid nitrogen and frozen at −80 °C. The NAD$^+$/NADH ratio was measured using a protocol adapted from the manual of the NAD/NADH-Glo Assay kit (Promega, G9072). To measure NAD$^+$, 20 µl of lysate was transferred to PCR tubes and diluted with 20 µl of lysis buffer and 20 µl 0.4 N HCl, and subsequently incubated at 60 °C for 15 min. For NADH measurement, 20 µl of freshly thawed lysate was transferred to PCR tubes and incubated at 75 °C for 30 min. The acidic conditions permit for selective degradation of NADH, while the basic conditions degrade NAD$^+$. Following the incubation, samples were spun on a bench-top centrifuge and quenched with 20 µl neutralizing solution. The neutralizing solution consisted of 0.5 M Tris base for NAD$^+$ samples and 0.25 M Tris in 0.2 N HCl for the NADH samples. The instructions in the Promega G9072 technical manual were then followed to measure NAD$^+$ and NADH levels using a luminometer (Tecan Infinite M200Pro).

Immunoblotting. Cells were washed with ice-cold PBS, and scraped into cold RIPA buffer containing cOmplete Mini protease inhibitor (Roche, 11836170001) and PhosStop Phosphatase Inhibitor Cocktail Tablets (Roche, 04906845001). Protein concentration was calculated using the BCA Protein Assay (Pierce, 23225) with BSA as a standard. Lysates were resolved by SDS–PAGE and proteins were transferred onto nitrocellulose membranes using the iBlot2 Dry Blotting System (Thermo Fisher, IB21001 and IB23001). Protein was detected with the primary antibodies anti-PDH E1-alpha subunit (phospho S232; 1:1,000 dilution; EMD Millipore, AP1063), anti-PDH E1-alpha subunit (1:1,000 dilution; phospho S293; Abcam, ab92696), anti-PDH E1-alpha subunit (phospho S300; 1:1,000 dilution; EMD Millipore, AP1064), anti-PDH E1-alpha subunit (total; 1:1,000 dilution; Proteintech, 18068-1-AP), anti-PDHK1 (1:1,000 dilution; Cell Signaling Technologies, C47H1), anti-PDP1 (1:1,000 dilution; Cell Signaling Technologies, D8Y6L), anti-FASN (1:1,000 dilution; Cell Signaling Technologies, 3180S), anti-ACC1 (1:1,000 dilution; Cell Signaling Technologies, 4190S), anti-ACC1 (1:1,000 dilution; phospho S79, Cell Signaling Technologies, 3661S) and anti-vinculin (1:1,000 dilution; Sigma, V9131). The secondary antibody used was anti-rabbit IgG horseradish peroxidase-linked antibody (1:5,000 dilution; Cell Signaling Technologies, 7074S).

Statistics and reproducibility. All statistical tests using experimental data were performed with Prism 8 software unless mentioned otherwise. FBA calculations were performed using MATLAB (version R2019a) and Gurobi Optimizer (version 8.1.1.). TCGA correlation analysis was performed in R (version 4.2.0). No statistical method was used to predetermine samples size. Sample sizes were chosen based on pilot experiments using three or more technical replicates. No data were excluded from the analyses. The experiments were not randomized and the investigators were not blinded to allocation during experiments and outcome assessment.

Reporting summary. Further information on research design is available in the Nature Research Reporting Summary linked to this article.

Data availability

Source data are provided with this paper.

Code availability

All code is available at https://github.com/kostyat/Lipid_synthesis/.

Received: 5 October 2020; Accepted: 17 May 2022;
Published online: 23 June 2022

References

1. Hosios, A. M. et al. Amino acids rather than glucose account for the majority of cell mass in proliferating mammalian cells. *Dev. Cell* **36**, 540–549 (2016).
2. Yao, C.-H. et al. Exogenous fatty acids are the preferred source of membrane lipids in proliferating fibroblasts. *Cell Chem. Biol.* **23**, 483–493 (2016).
3. Jain, M. et al. Metabolite profiling identifies a key role for glycine in rapid cancer cell proliferation. *Science* **336**, 1040 (2012).
4. Damaraju, V. L. et al. Nucleoside anticancer drugs: the role of nucleoside transporters in resistance to cancer chemotherapy. *Oncogene* **22**, 7524–7536 (2003).
5. Muir, A., Danai, L. V. & Vander Heiden, M. G. Microenvironmental regulation of cancer cell metabolism: implications for experimental design and translational studies. *Dis. Models Mech.* **11**, dmm035758–12 (2018).
6. Sullivan, M. R. et al. Quantification of microenvironmental metabolites in murine cancers reveals determinants of tumor nutrient availability. *Elife* **8**, e44235 (2019).

7. Vaupel, P., Kallinowski, F. & Okunieff, P. Blood flow, oxygen and nutrient supply, and metabolic microenvironment of human tumors: a review. *Cancer Res.* **49**, 6449 (1989).
8. Eales, K. L., Hollinshead, K. E. R. & Tennant, D. A. Hypoxia and metabolic adaptation of cancer cells. *Oncogenesis* **5**, e190–8 (2016).
9. Hu, J. et al. Heterogeneity of tumor-induced gene expression changes in the human metabolic network. *Nat. Biotechnol.* **31**, 522–529 (2013).
10. Gui, D. Y. et al. Environment dictates dependence on mitochondrial complex I for NAD+ and aspartate Production and determines cancer cell sensitivity to metformin. *Cell Metab.* **24**, 716–727 (2016).
11. Sullivan, L. B. et al. Supporting aspartate biosynthesis is an essential function of respiration in proliferating cells. *Cell* **162**, 552–563 (2015).
12. Sullivan, L. B. et al. Aspartate is an endogenous metabolic limitation for tumour growth. *Nat. Cell Biol.* **20**, 1–12 (2018).
13. Birsoy, K. et al. An essential role of the mitochondrial electron transport chain in cell proliferation is to enable aspartate synthesis. *Cell* **162**, 540–551 (2015).
14. Garcia-Bermudez, J. et al. Aspartate is a limiting metabolite for cancer cell proliferation under hypoxia and in tumours. *Nat. Cell Biol.* **20**, 1–12 (2018).
15. Fernandez-de-Cossio-Diaz, J. & Vazquez, A. Limits of aerobic metabolism in cancer cells. *Sci. Rep.* **7**, 13488 (2017).
16. Titov, D. V. et al. Complementation of mitochondrial electron transport chain by manipulation of the NAD+/NADH ratio. *Science* **352**, 231–235 (2016).
17. Diehl, F. F., Lewis, C. A., Fiske, B. P. & Vander Heiden, M. G. Cellular redox state constrains serine synthesis and nucleotide production to impact cell proliferation. *Nat. Metab.* **1**, 861–867 (2019).
18. Bao, X. R. et al. Mitochondrial dysfunction remodels one-carbon metabolism in human cells. *Elife* **5**, e10575 (2016).
19. Murphy, J. P. et al. The NAD+ salvage pathway supports PHGDH-driven serine biosynthesis. *Cell Rep.* **24**, 2381–2391 (2018).
20. Kim, W. et al. Polyunsaturated fatty acid desaturation is a mechanism for glycolytic NAD+ recycling. *Cell Metab.* 1–42 (2019).
21. Price, N. C. & Stevens, L. *Fundamentals of Enzymology* (Oxford University Press, 2000).
22. Los, D. A. & Murata, N. Structure and expression of fatty acid desaturases. *Biochim. Biophys. Acta* **1394**, 3–15 (1998).
23. Park, S. H. et al. Phosphorylation-activity relationships of AMPK and acetyl-CoA carboxylase in muscle. *J. Appl. Physiol.* **92**, 2475–2482 (2002).
24. Schulz, H. Beta oxidation of fatty acids. *Biochim. Biophys. Acta* **1081**, 109–120 (1991).
25. Kamphorst, J. J. et al. Hypoxic and Ras-transformed cells support growth by scavenging unsaturated fatty acids from lysophospholipids. *Proc. Natl Acad. Sci. USA* **110**, 8882 (2013).
26. Ackerman, D. et al. Triglycerides promote lipid homeostasis during hypoxic stress by balancing fatty acid saturation. *Cell Rep.* **24**, 2596–2605 (2018).
27. Bensaad, K. et al. Fatty acid uptake and lipid storage induced by HIF-1α contribute to cell growth and survival after hypoxia-reoxygenation. *Cell Rep.* **9**, 349–365 (2014).
28. Jain, I. H. et al. Genetic screen for cell fitness in high or low oxygen highlights mitochondrial and lipid metabolism. *Cell* **181**, 716–727 (2020).
29. Luengo, A. et al. Increased demand for NAD+ relative to ATP drives aerobic glycolysis. *Mol. Cell* **81**, 691–707 (2021).
30. Harris, A. L. Hypoxia—a key regulatory factor in tumour growth. *Nat. Rev. Cancer* **2**, 38–47 (2002).
31. Wise, D. R. et al. Hypoxia promotes isocitrate dehydrogenase-dependent carboxylation of α-ketoglutarate to citrate to support cell growth and viability. *Proc. Natl Acad. Sci. USA* **108**, 19611–19616 (2011).
32. Metallo, C. M. et al. Reductive glutamine metabolism by IDH1 mediates lipogenesis under hypoxia. *Nature* **481**, 380–384 (2012).
33. Mullen, A. R. et al. Reductive carboxylation supports growth in tumour cells with defective mitochondria. *Nature* **481**, 385–388 (2011).
34. Dupuy, F. et al. PDK1-dependent metabolic reprogramming dictates metastatic potential in breast cancer. *Cell Metab.* **22**, 577–589 (2015).
35. Duarte, N. C. et al. Global reconstruction of the human metabolic network based on genomic and bibliomic data. *Proc. Natl Acad. Sci. USA* **104**, 1777–1782 (2007).
36. Orth, J. D., Thiele, I. & Palsson, B. Ø. What is flux balance analysis? *Nat. Biotechnol.* **28**, 245–248 (2010).
37. Jerby, L., Shlomi, T. & Ruppin, E. Computational reconstruction of tissue-specific metabolic models: application to human liver metabolism. *Mol. Syst. Biol.* **6**, 401 (2010).
38. Zielinski, D. C. et al. Systems biology analysis of drivers underlying hallmarks of cancer cell metabolism. *Sci. Rep.* **7**, 41241 (2017).
39. Saggerson, E. D. The regulation of glyceride synthesis in isolated white-fat cells. The effects of acetate, pyruvate, lactate, palmitate, electron-acceptors, uncoupling agents and oligomycin. *Biochem. J.* **128**, 1069–1078 (1972).
40. Wise, E. M. Jr & Ball, E. G. Malic enzyme and lipogenesis. *Proc. Natl Acad. Sci. USA* **52**, 1255–1263 (1964).
41. Liu, L. et al. Malic enzyme tracers reveal hypoxia-induced switch in adipocyte NADPH pathway usage. *Nat. Chem. Biol.* **12**, 345–352 (2016).
42. Hosios, A. M. & Vander Heiden, M. G. The redox requirements of proliferating mammalian cells. *J. Biol. Chem.* **293**, 7490–7498 (2018).
43. DeBerardinis, R. J. et al. Beyond aerobic glycolysis: transformed cells can engage in glutamine metabolism that exceeds the requirement for protein and nucleotide synthesis. *Proc. Natl Acad. Sci. USA* **104**, 19345 (2007).
44. Santos, C. R. & Schulze, A. Lipid metabolism in cancer. *FEBS J.* **279**, 2610–2623 (2012).
45. Hosios, A., Li, Z., Lien, E. & Vander Heiden, M. Preparation of lipid-stripped serum for the study of lipid metabolism in cell culture. *Bio. Protoc.* **8**, e2876 (2018).
46. Gameiro, P. A. et al. In vivo HIF-mediated reductive carboxylation is regulated by citrate levels and sensitizes VHL-deficient cells to glutamine deprivation. *Cell Metab.* **17**, 372–385 (2013).
47. Kaplon, J. et al. A key role for mitochondrial gatekeeper pyruvate dehydrogenase in oncogene-induced senescence. *Nature* **498**, 109–112 (2013).
48. Linn, T. C., Pettit, F. H. & Reed, L. J. α-keto acid dehydrogenase complexes, X. Regulation of the activity of pyruvate dehydrogenase complex from beef kidney mitochondria by phosphorylation and dephosphorylation. *Proc. Natl Acad. Sci. USA* **62**, 234–241 (1969).
49. Schell, J. C. et al. A role for the mitochondrial pyruvate carrier as a repressor of the Warburg effect and colon cancer cell growth. *Mol. Cell* **56**, 400–413 (2014).
50. Vacanti, N. M. et al. Regulation of substrate utilization by the mitochondrial pyruvate carrier. *Mol. Cell* **56**, 425–435 (2014).
51. Yang, C. et al. Glutamine oxidation maintains the TCA cycle and cell survival during impaired mitochondrial pyruvate transport. *Mol. Cell* **56**, 414–424 (2014).
52. Bricker, D. K. et al. A mitochondrial pyruvate carrier required for pyruvate uptake in yeast, *Drosophila* and humans. *Science* **337**, 96–100 (2012).
53. Herzig, S. et al. Identification and functional expression of the mitochondrial pyruvate carrier. *Science* **337**, 93–96 (2012).
54. Fendt, S.-M. et al. Reductive glutamine metabolism is a function of the α-ketoglutarate-to-citrate ratio in cells. *Nat. Commun.* **4**, 2236 (2013).
55. Owen, M. R., Doran, E. & Halestrap, A. P. Evidence that metformin exerts its anti-diabetic effects through inhibition of complex 1 of the mitochondrial respiratory chain. *Biochem. J.* **348**, 607–614 (2000).
56. Bücher, T. et al. State of oxidation–reduction and state of binding in the cytosolic NADH-system as disclosed by equilibration with extracellular lactate/pyruvate in hemoglobin-free perfused rat liver. *Eur. J. Biochem.* **27**, 301–317 (1972).
57. Hung, Y. P., Albeck, J. G., Tantama, M. & Yellen, G. Imaging cytosolic NADH–NAD+ redox state with a genetically encoded fluorescent biosensor. *Cell Metab.* **14**, 545–554 (2011).
58. Hatzivassiliou, G. et al. ATP citrate lyase inhibition can suppress tumor cell growth. *Cancer Cell* **8**, 311–321 (2005).
59. Faubert, B. et al. Lactate metabolism in human lung tumors. *Cell* **171**, 358–371 (2017).
60. Hui, S. et al. Glucose feeds the TCA cycle via circulating lactate. *Nature* **551**, 115–118 (2017).
61. Zhao, Y. et al. In vivo monitoring of cellular energy metabolism using SoNar, a highly responsive sensor for NAD+/NADH redox state. *Nat. Protoc.* **11**, 1345–1359 (2016).
62. Garcia, D. & Shaw, R. J. AMPK: mechanisms of cellular energy sensing and restoration of metabolic balance. *Mol. Cell* **66**, 789–800 (2017).
63. Latasa, M. J., Moon, Y. S., Kim, K. H. & Sul, H. S. Nutritional regulation of the fatty acid synthase promoter in vivo: sterol regulatory element binding protein functions through an upstream region containing a sterol regulatory element. *Proc. Natl Acad. Sci. USA* **97**, 10619–10624 (2000).
64. Lewis, C. A. et al. SREBP maintains lipid biosynthesis and viability of cancer cells under lipid- and oxygen-deprived conditions and defines a gene signature associated with poor survival in glioblastoma multiforme. *Oncogene* **34**, 5128–5140 (2015).
65. Comerford, S. A. et al. Acetate dependence of tumors. *Cell* **159**, 1591–1602 (2014).
66. Mashimo, T. et al. Acetate Is a bioenergetic substrate for human glioblastoma and brain metastases. *Cell* **159**, 1603–1614 (2014).
67. Schug, Z. T. et al. Acetyl-CoA synthetase 2 promotes acetate utilization and maintains cancer cell growth under metabolic stress. *Cancer Cell* **27**, 57–71 (2015).
68. Bulusu, V. et al. Acetate recapturing by nuclear acetyl-CoA synthetase 2 prevents loss of histone acetylation during oxygen and serum limitation. *Cell Rep.* **18**, 647–658 (2017).
69. Liu, X. et al. Acetate production from glucose and coupling to mitochondrial metabolism in mammals. *Cell* **175**, 502–513 (2018).
70. Röhrig, F. & Schulze, A. The multifaceted roles of fatty acid synthesis in cancer. *Nat. Rev. Cancer* **16**, 732–749 (2016).

71. Jones, M. E., Lipmann, F., Hilz, H. & Lynen, F. On the enzymatic mechanism of coenzyme A acetylation with adenosine triphosphate and acetate. *J. Am. Chem. Soc.* **75**, 3285–3286 (1953).
72. Kanehisa, M. & Goto, S. KEGG: Kyoto Encyclopedia of Genes and Genomes. *Nucleic Acids Res.* **28**, 27–30 (2000).
73. Mense, S. M. et al. Gene expression profiling reveals the profound upregulation of hypoxia-responsive genes in primary human astrocytes. *Physiol. Genomics* **25**, 435–449 (2006).
74. Horton, J. D., Goldstein, J. L. & Brown, M. S. SREBPs: activators of the complete program of cholesterol and fatty acid synthesis in the liver. *J. Clin. Invest.* **109**, 1125–1131 (2002).
75. Davidson, S. M. et al. Environment impacts the metabolic dependencies of Ras-driven non-small cell lung cancer. *Cell Metab.* **23**, 517–528 (2016).
76. Davidson, S. M. et al. Direct evidence for cancer-cell-autonomous extracellular protein catabolism in pancreatic tumors. *Nat. Med.* **23**, 235–241 (2017).
77. Sullivan, M. R. et al. Increased serine synthesis provides an advantage for tumors arising in tissues where serine levels are limiting. *Cell Metab.* **29**, 1410–1421 (2019).
78. Savino, A. M. et al. Metabolic adaptation of acute lymphoblastic leukemia to the central nervous system microenvironment depends on stearoyl-CoA desaturase. *Nat. Cancer* **1**, 998–1009 (2020).
79. Jin, X. et al. A metastasis map of human cancer cell lines. *Nature* **588**, 331–336 (2020).
80. Summons, R. E., Bradley, A. S., Jahnke, L. L. & Waldbauer, J. R. Steroids, triterpenoids and molecular oxygen. *Philos. Trans. R. Soc. Lond. B Biol. Sci.* **361**, 951–968 (2006).
81. Maddocks, O. D. K. et al. Modulating the therapeutic response of tumours to dietary serine and glycine starvation. *Nature* **544**, 372–376 (2017).
82. Li, L. et al. Identification of DHODH as a therapeutic target in small-cell lung cancer. *Sci. Transl. Med.* **11**, eaaw7852 (2019).
83. Sousa, C. M. et al. Pancreatic stellate cells support tumour metabolism through autophagic alanine secretion. *Nature* **536**, 479–483 (2016).
84. Parker, S. J. et al. Selective alanine transporter utilization creates a targetable metabolic niche in pancreatic cancer. *Cancer Discov.* **10**, 1018–1037 (2020).
85. Hsueh, E. C. et al. Deprivation of arginine by recombinant human arginase in prostate cancer cells. *J. Hematol. Oncol.* **5**, 17 (2012).

Acknowledgements

We thank the members of the D.V. and M.G.V.H. laboratories for helpful discussions. The results published here are in part based upon data generated by the TCGA Research Network. This work was supported by the National Institutes of Health (NIH) grants R01CA201276 (to D.V. and M.G.V.H.) and T32GM007367 (to B.W.J.), the MD-PhD program at Columbia University (to B.W.J.) and NIH grants U54CA209997 (to P.D., K.T., B.W.J. and D.V.) and T32GM007287 (Z.L. and K.L.A.). E.C.L. is a Damon Runyon Fellow supported by the Damon Runyon Cancer Research Foundation (DRG-2299-17). A.M.H. was supported by an HHMI International Student Fellowship. J.C.R. is supported by the Harvard/MIT MD-PhD Program NIH award T32GM007753. L.B.S. acknowledges support from a Pathway to Independence award from the NIH (K99CA218679/R00CA218679). E.F.G. was supported by the MIT MSRP program. M.G.V.H. also acknowledges support from the Lustgarten Foundation, SU2C, the Ludwig Center at MIT, the NCI (R35CA242379 and P30CA014051), the MIT Center for Precision Cancer Medicine, the Emerald Foundation and a Faculty Scholar award from HHMI. The content is solely the responsibility of the authors and does not necessarily represent the official views of the National Cancer Institute or the NIH.

Author contributions

B.W.J, Z.L., P.D.D., M.G.V.H. and D.V. conceived the study. Z.L., B.W.J., P.D.D., K.T., M.G.V.H. and D.V. wrote the manuscript. B.W.J., K.T. and P.D.D. developed and executed the computation analysis of global metabolic flux and NAD^+ costs analysis. Z.L., A.M.H., E.F.G., K.L.A. and L.B.S. performed proliferation assays. Z.L. performed oxygen consumption assays. Z.L. and E.C.L. performed serum delipidation. Z.L. performed kinetic isotope tracing and lipid synthesis assays. Z.L. and J.C.R. performed immunoblot assays. Z.L and A.M.W. performed NAD^+ measurement assays. Z.L. performed mass spectrometry and analysis for metabolites. Z.L. generated cell lines used for this study. B.W.J., K.T. and P.D.D. performed TCGA analysis of gene expression correlations. M.G.V.H. and D.V. supervised the project.

Competing interests

A.M.W. is a current employee of Revitope. M.G.V.H. is a consultant and scientific advisor for Agios Pharmaceuticals, iTeos Therapeutics, Droia Ventures, Faeth Therapeutics, Sage Therapeutics and Auron Therapeutics. All other authors declare no competing interests.

Additional information

Extended data is available for this paper at https://doi.org/10.1038/s42255-022-00588-8.

Supplementary information The online version contains supplementary material available at https://doi.org/10.1038/s42255-022-00588-8.

Correspondence and requests for materials should be addressed to Matthew G. Vander Heiden or Dennis Vitkup.

Peer review information *Nature Metabolism* thanks Navdeep Chandel and the other, anonymous, reviewers for their contribution to the peer review of this work. Primary Handling Editors: Alfredo Gimenez-Cassina and George Caputa, in collaboration with the *Nature Metabolism* team.

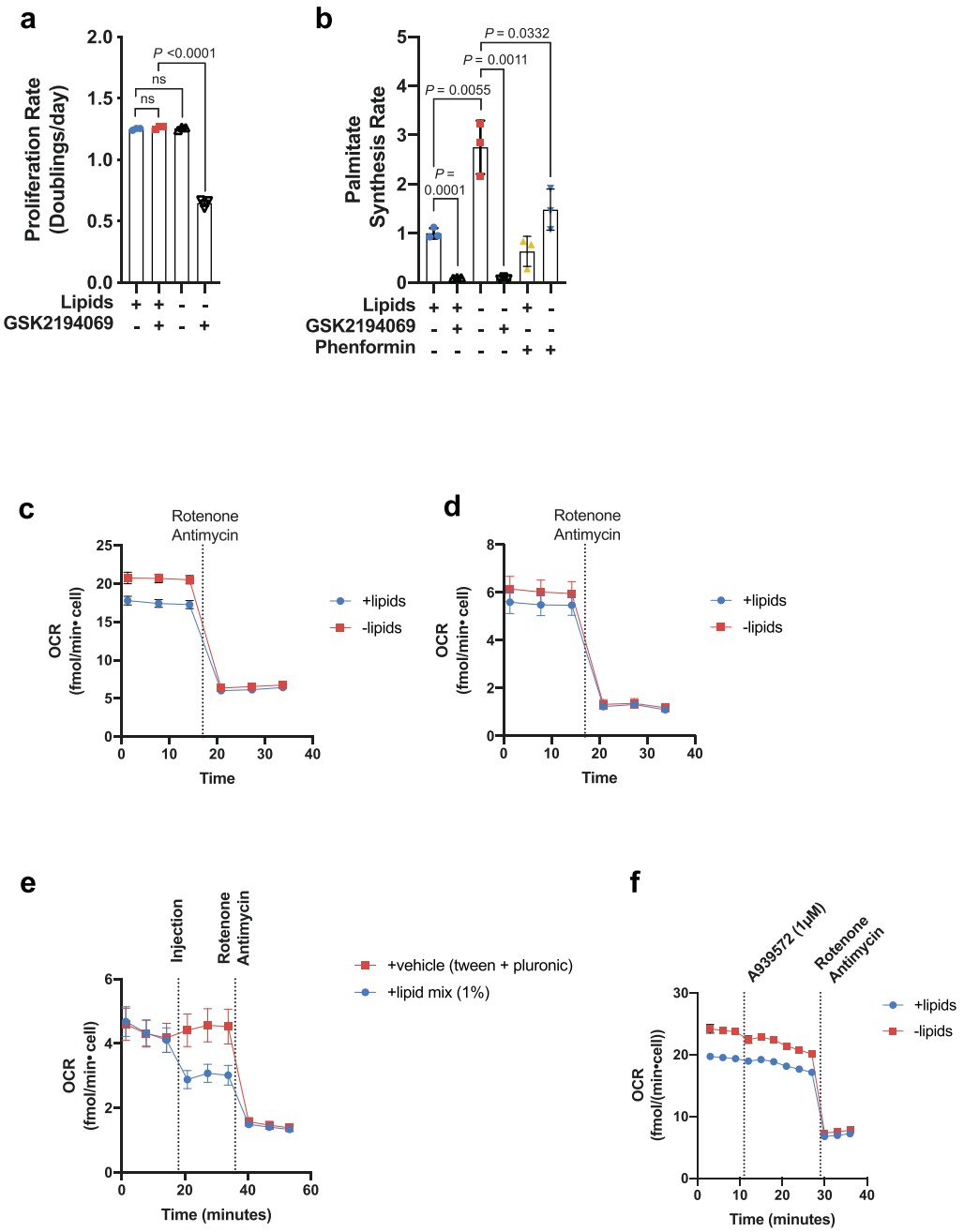

Extended Data Fig. 1 | Effects of lipid depletion and fatty acid synthesis inhibition on cell proliferation. a, Cell culture media was prepared with delipidated serum, and then reconstituted with 1% Lipid Mixture (2 μg/ml arachidonic and 10 μg/ml each linoleic, linolenic, myristic, oleic, palmitic and stearic acid, and 0.22 mg/ml cholesterol) (+lipids) or vehicle (−lipids). Proliferation rates of HeLa cells cultured in media +lipids or −lipids without and with the FASN inhibitor GSK2194069 (0.3 μM) as indicated ($n = 3$ per condition from a representative experiment). **b**, Relative palmitate synthesis rates of HeLa cells cultured in media +lipids or −lipids without and with GSK2194069 (0.3 μM), or without and with phenformin (100 μM) as indicated ($n = 3$ per condition from a representative experiment). **c**, Oxygen consumption rate (OCR) of HeLa cells cultured in media +lipids or −lipids as indicated ($n = 10$ per condition from a representative experiment). **d**, OCR of H1299 cells cultured in media +lipids or −lipids as indicated ($n = 10$ per condition from a representative experiment). **e**, OCR of H1299 cells cultured in −lipid and acutely treated with 1% Lipid Mixture or Tween-80 and Pluronic F-68 equivalent to what is present in 1% Lipid Mixture ($n = 10$ per condition from a representative experiment). **f**, OCR of HeLa cell cultures in media +lipids or −lipids acutely treated with the SCD1 inhibitor A939572 (1 μM) and rotenone (1.5 μM) + antimycin A (1.5 μM) as indicated ($n = 8$ per condition from a representative experiment). All bar charts and line graphs show means with error bars representing ± s.d. Unpaired Student's *t*-test was performed where statistics are shown. All experiments were repeated three times or more.

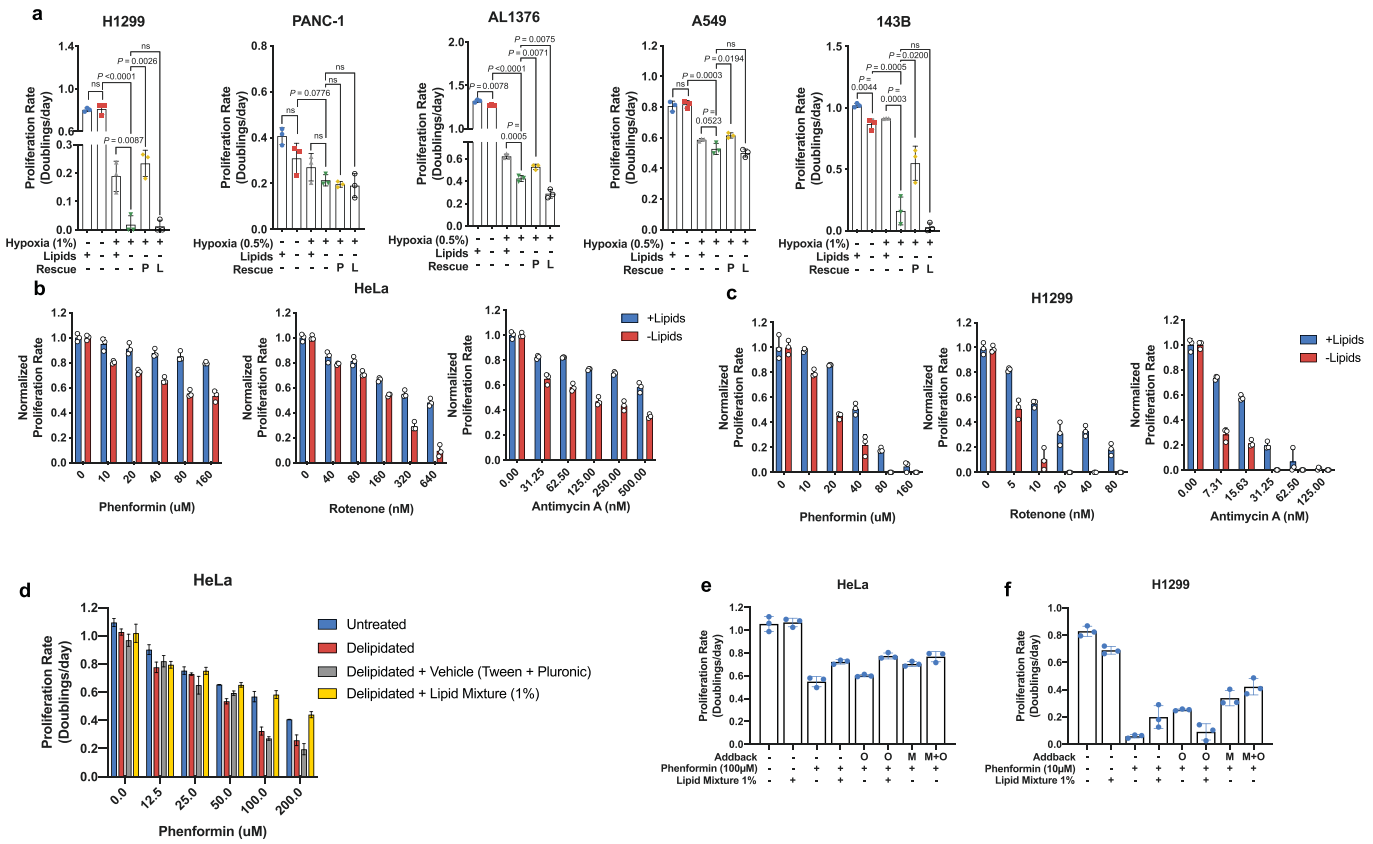

Extended Data Fig. 2 | Electron acceptor availability dictates proliferation rate in the absence of exogenous lipids. a, Proliferation rates of H1299, PANC-1, AL1376, A549, and 143B cells cultured in media +lipids or −lipids in normoxia (21% oxygen) or hypoxia (0.5% or 1% oxygen), without or with pyruvate (1 mM, P) and/or lactate (10 mM, L) as indicated ($n = 3$ per condition from a representative experiment). **b**, Proliferation rate of HeLa cells cultured in media +lipids or −lipids with a titration of phenformin (Complex I inhibitor), rotenone (Complex I inhibitor), or antimycin A (Complex III inhibitor) as indicated ($n = 3$ per condition from a representative experiment). **c**, Proliferation rate of H1299 cells cultured in media +lipids or −lipids with a titration of phenformin, rotenone, or antimycin A as indicated ($n = 3$ per condition from a representative experiment). **d**, Proliferation rates of HeLa cells cultured in media containing the indicated doses of Phenformin with dialyzed fetal bovine serum that has been untreated, delipidated and reconstituted with 1% Lipid Mixture (2 μg/ml arachidonic and 10 μg/ml each linoleic, linolenic, myristic, oleic, palmitic and stearic acid, and 0.22 mg/ml cholesterol), or delipidated and reconstituted with Tween-80 and Pluronic F-68 equivalent to what is present in 1% Lipid Mixture ($n = 3$ per condition from a representative experiment). **e**, Proliferation rates of HeLa cells cultured in media −lipids treated with phenformin (100 μM), when indicated, and supplemented with either 1% Lipid Mixture or the equivalent amounts of oleate (O) and/or mevalonate (M) found in 1% Lipid Mixture ($n = 3$ per condition from a representative experiment). **f**, Proliferation rates of H1299 cells cultured in media −lipids treated with phenformin (10 μM), when indicated, and supplemented with either 1% Lipid Mixture or the equivalent amounts of oleate (O) and/or mevalonate (M) found in 1% Lipid Mixture ($n = 3$ per condition from a representative experiment). All bar charts show means with error bars representing ± s.d. Unpaired Student's *t*-test was performed where statistics are shown. All experiments were repeated three times or more.

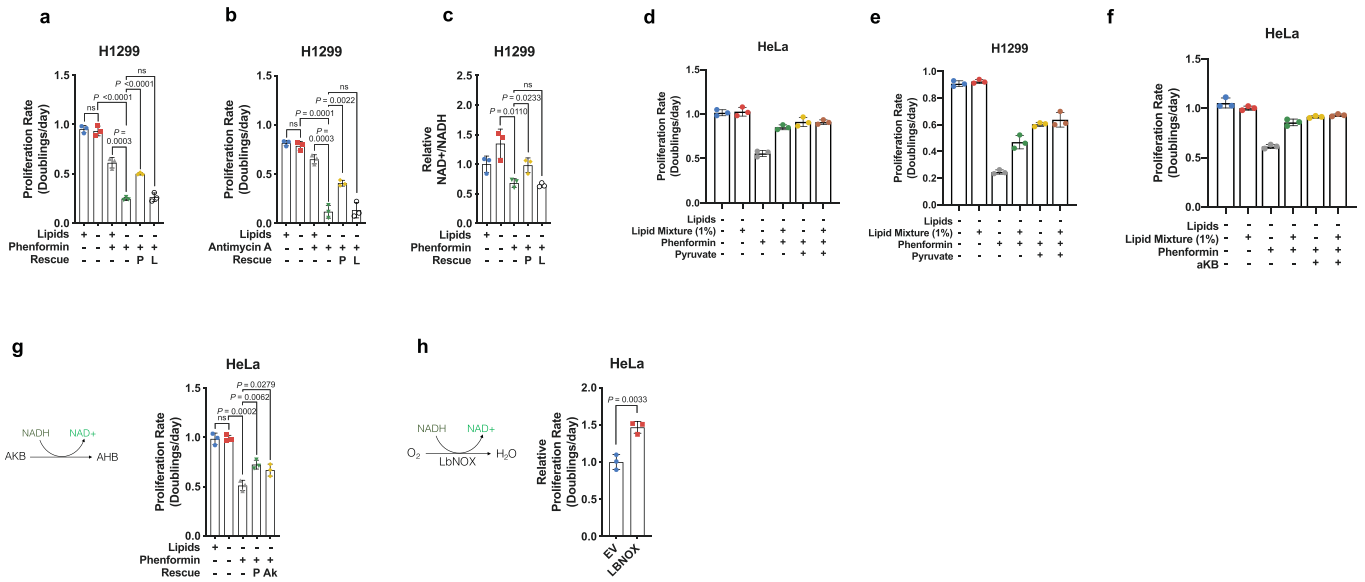

Extended Data Fig. 3 | Orthogonal mechanisms of electron acceptor regeneration restore lipid synthesis under ETC inhibition. a, Proliferation rates of H1299 cells cultured in media +lipids or −lipids, without or with phenformin (10 μM), pyruvate (1 mM, P), and/or lactate (10 mM, L) as indicated ($n = 3$ per condition from a representative experiment). **b**, Proliferation rates of H1299 cells cultured in media +lipids or −lipids without or with antimycin A (15 nM), pyruvate (1 mM, P), and/or lactate (10 mM, L) as indicated ($n = 3$ per condition from a representative experiment). **c**, Relative NAD+ /NADH ratio in H1299 cells cultured in media +lipids or −lipids without or with phenformin (10 μM), pyruvate (1 mM, P), and/or lactate (10 mM, L) as indicated ($n = 3$ per condition from a representative experiment). **d**, Proliferation rates of HeLa cells cultured in medium −lipids without or with 1% Lipid Mixture, phenformin (100 μM), and/or pyruvate (1 mM, P), as indicated ($n = 3$ per condition from a representative experiment). **e**, Proliferation rates of H1299 cells cultured in medium −lipids without or with 1% Lipid Mixture, phenformin (10 μM), and/or pyruvate (1 mM, P), as indicated ($n = 3$ per condition from a representative experiment). **f**, Proliferation rates of HeLa cells cultured in medium −lipids without or with 1% Lipid Mixture, phenformin (100 μM), and/or α-ketobutyrate (1 mM, αKB), as indicated ($n = 3$ per condition from a representative experiment). **g**, Proliferation rates of HeLa cells cultured in media +lipids or −lipids without or with phenformin (100 μM), pyruvate (1 mM, P), and/or alpha-ketobutyrate (1 mM, Ak) as indicated ($n = 3$ per condition from a representative experiment). **h**, Relative proliferation rates of HeLa cells expressing empty vector (EV) or *lb*NOX cultured in −lipids with phenformin (100 μM) as indicated. Data were normalized to HeLa-EV cells ($n = 3$ per condition from a representative experiment). All bar charts show means with error bars representing ± s.d. Unpaired Student's *t*-test was performed where statistics are shown. All experiments were repeated three times or more.

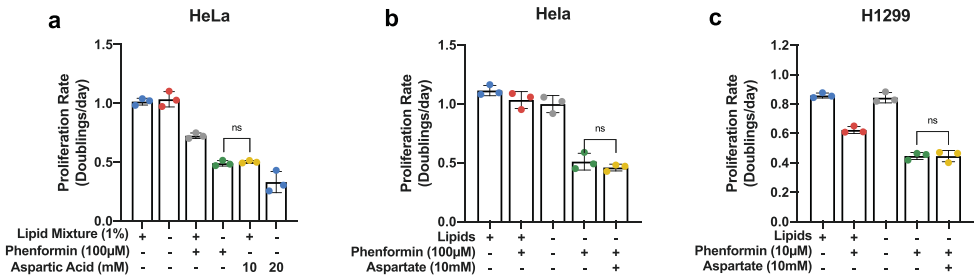

Extended Data Fig. 4 | Effects of aspartate on proliferation in the absence of lipids. a, Proliferation rates of HeLa cells cultured in media +lipids or −lipids, without or with phenformin (100 μM), and/or aspartic acid (10 mM or 20 mM) as indicated ($n = 3$ per condition from a representative experiment). **b**, Proliferation rates of HeLa cells cultured in media +lipids or −lipids, without or with phenformin (100 μM), and/or sodium aspartate (10 mM) as indicated ($n = 3$ per condition from a representative experiment). **c**, Proliferation rates of H1299 cells cultured in media +lipids or −lipids, without or with phenformin (10 μM), and/or sodium aspartate (10 mM) as indicated ($n = 3$ per condition from a representative experiment). All bar charts show means with error bars representing ± s.d. Unpaired Student's *t*-test was performed where statistics are shown. All experiments were repeated three times or more.

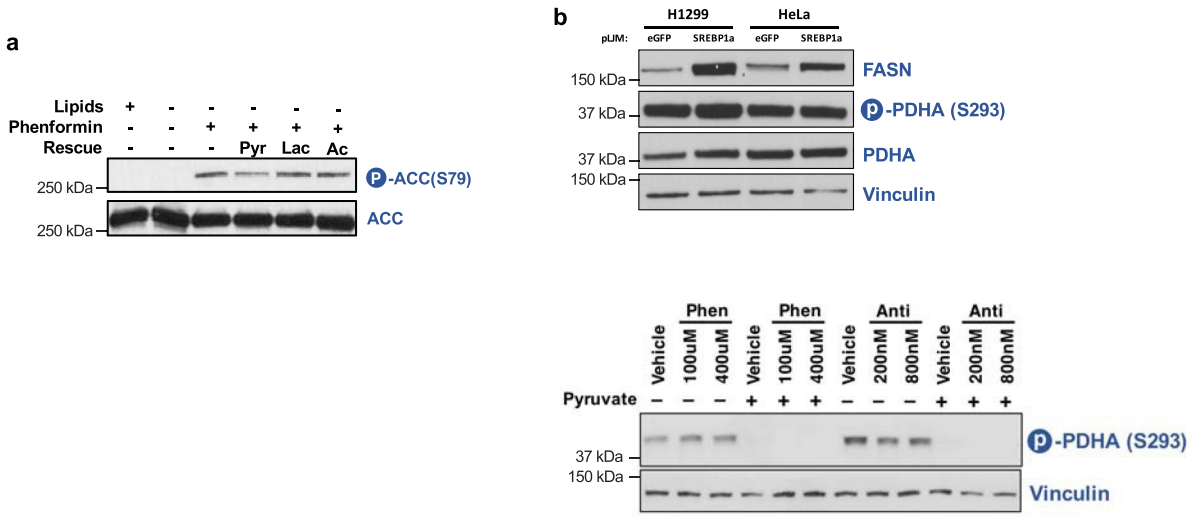

Extended Data Fig. 5 | Effects of exogenous metabolites on ACC phosphorylation. a, Representative immunoblot of total ACC and ACC serine 79 phosphorylation in HeLa cells cultured for 24 hours in media +lipids or –lipids without or with phenformin (100 μM), pyruvate (1 mM, Pyr), lactate (10 mM, Lac), and/or acetate (200 μM, Ac) as indicated. **b**, (top) Representative immunoblot of FASN, phosphorylated PDHA (Serine 293), total PDHA, and vinculin in HeLa or H1299 cells overexpressing eGFP or constitutively mature SREBP1a. (bottom) Representative immunoblot of phosphorylated PDHA (Serine 293) and Vinculin in HeLa cultured in –lipids for 24hrs, treated with vehicle, phenformin, antimycin, pyruvate, and/or alpha-ketobutyrate at the indicated doses. All experiments were repeated three times or more.

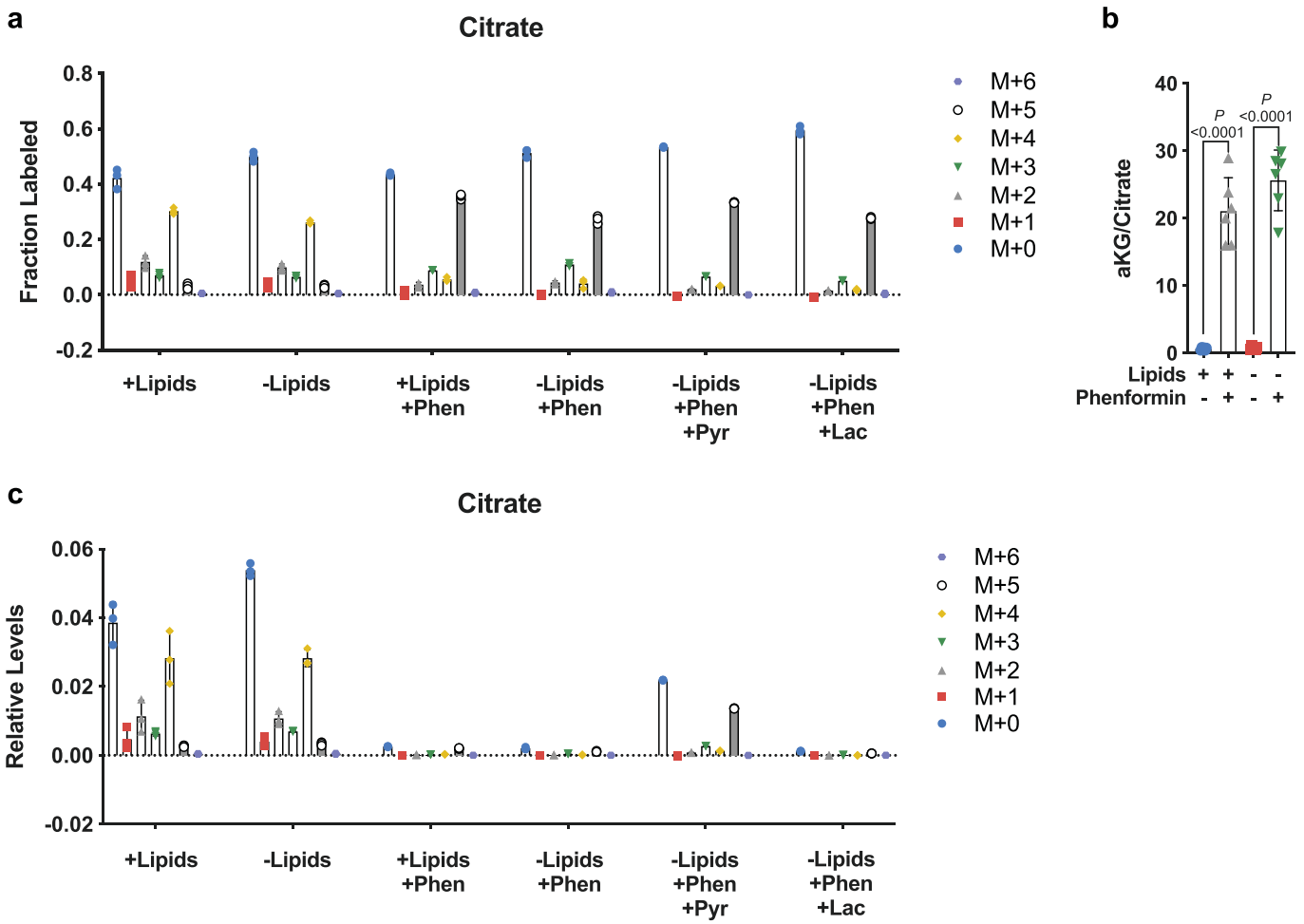

Extended Data Fig. 6 | Inhibition of mitochondrial electron transport decreases intracellular citrate levels. a, Relative fractional distribution of citrate isotopomers in HeLa cells cultured for 24 hours in media +lipids or −lipids with U-^{13}C-Glutamine, without and with phenformin (100 μM), pyruvate (1 mM, Pyr), and/or lactate (10 mM, Lac) as indicated ($n = 3$ per condition from a representative experiment). **b**, Normalized intracellular ratio of αKG to citrate in HeLa cells cultured in +lipids or −lipids with or without phenformin (100 μM). ($n = 6$ per condition from a representative experiment). **c**, Isotopomer distribution of total levels of intracellular citrate in HeLa cells cultured for 24 hours in media +lipids or −lipids with U-^{13}C-Glutamine, without and with phenformin (100 μM), pyruvate (1 mM, Pyr), and/or lactate (10 mM, Lac) as indicated ($n = 3$ per condition from a representative experiment). All bar charts show means with error bars representing ± s.d. Unpaired Student's *t*-test was performed where statistics are shown. All experiments were repeated three times or more. ($n = 3$ per condition from a representative experiment).

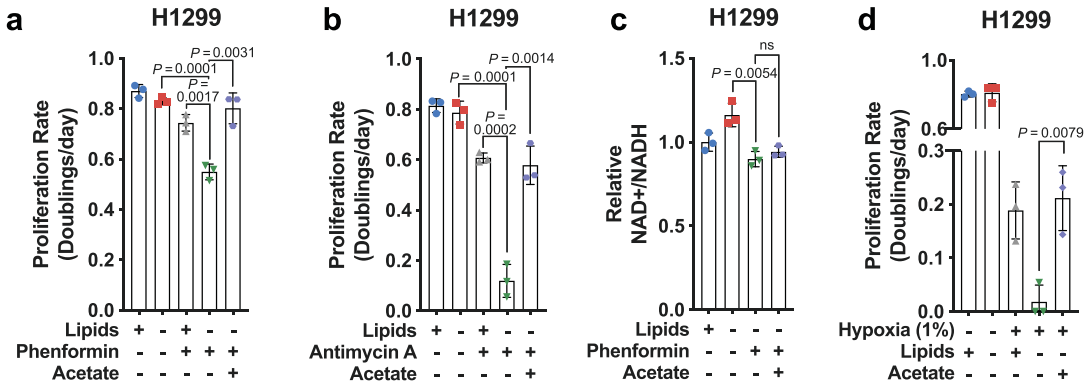

Extended Data Fig. 7 | Bypassing oxidative steps in fatty acid synthesis rescues proliferation in electron acceptor-deficient cells. a, Proliferation rates of H1299 cells cultured in media +lipids or −lipids without or with phenformin (10 μM) and/or acetate (200 μM) as indicated ($n = 3$ per condition from a representative experiment). **b**, Proliferation rates of H1299 cells cultured in media +lipids or −lipids without or with antimycin A (15 nM) and/or acetate (200 μM) as indicated ($n = 3$ per condition from a representative experiment). **c**, Relative NAD+ /NADH ratio in H1299 cells cultured in media +lipids or −lipids without or with phenformin (10 μM) and/or acetate (200 μM) as indicated ($n = 3$ per condition from a representative experiment). **d**, Proliferation rates of H1299 cells cultured in media +lipids or −lipids in normoxia (21% oxygen), hypoxia (1% oxygen), and/or acetate (200 μM) as indicated. Data from the first four conditions are the same as those presented in Extended Data Fig. 2a. ($n = 3$ per condition from a representative experiment). All bar charts show means with error bars representing ± s.d. Unpaired Student's *t*-test was performed where statistics are shown. All experiments were repeated three times or more.

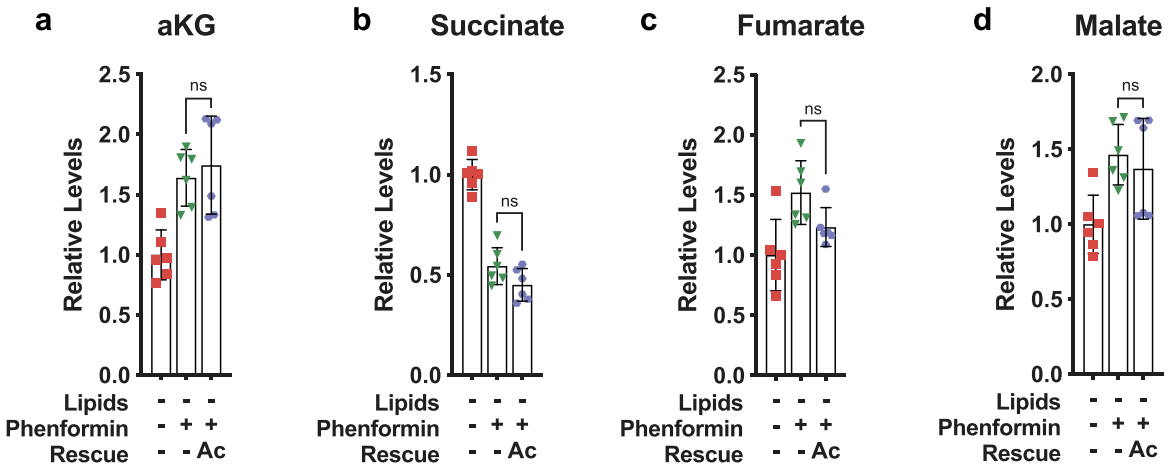

Extended Data Fig. 8 | Effect of exogenous acetate on levels of TCA cycle intermediates. a, Relative intracellular alpha-ketoglutarate (αKG) levels in HeLa cells cultured for 24 hours in medium –lipids without or with phenformin (100 μM) and/or acetate (200 μM) as indicated ($n = 6$ per condition from a representative experiment). **b**, Relative intracellular succinate levels in HeLa cells cultured for 24 hours in medium –lipids without or with phenformin (100 μM) and/or acetate (200 μM) as indicated ($n = 6$ per condition from a representative experiment). **c**, Relative intracellular fumarate levels in HeLa cells for 24 hours in medium –lipids without or with phenformin (100 μM) and/or acetate (200 μM) ($n = 6$ per condition from a representative experiment). **d**, Relative intracellular malate levels in HeLa cells cultured for 24 hours in medium –lipids without or with phenformin (100 μM) and/or acetate (200 μM) ($n = 6$ per condition from a representative experiment). All bar charts show means with error bars representing ± s.d. Unpaired Student's *t*-test was performed where statistics are shown. All experiments were repeated three times or more.

a

TUMOR TYPES	FULL NAME	Correlation between hypoxia and lipid synthesis	p value (log 10) (red values are insignificant)	Correlation between hypoxia and lipid uptake	p value (log 10) (red values are insignificant)	correlation between hypoxia and beta-oxidation	p value (log 10) (red values are insignificant)
ACC	Adenoid cystic carcinoma	-0.127	-0.579	0.278	-1.882	-0.296	-2.090
BLCA	Bladder Urothelial Carcinoma	-0.474	-23.474	0.176	-3.456	-0.385	-15.176
BRCA	Breast invasive carcinoma	-0.256	-17.114	0.490	-66.473	-0.063	-1.438
CESC	Cervical squamous cell carcinoma and endocervical adenocarcinoma	-0.197	-3.273	-0.013	-0.083	-0.174	-2.636
CHOL	Cholangiocarcinoma	-0.430	-2.051	0.341	-1.377	-0.056	-0.127
COAD	Colon adenocarcinoma	-0.366	-9.733	0.375	-10.231	-0.295	-6.391
COADREAD	Colorectal adenocarcinoma	-0.382	-13.853	0.405	-15.664	-0.300	-8.600
DLBC	Lymphoid Neoplasm Diffuse Large B-cell Lymphoma	-0.052	-0.141	0.465	-3.062	-0.013	-0.031
ESCA	Esophageal carcinoma	-0.495	-12.059	-0.094	-0.694	-0.559	-15.762
GBM	Glioblastoma multiforme	-0.292	-3.593	0.593	-15.154	-0.133	-0.989
GBMLGG	Glioma	-0.513	-45.459	0.764	-128.377	0.079	-1.382
HNSC	Head and Neck squamous cell carcinoma	-0.382	-18.804	0.260	-8.768	-0.193	-5.032
KIPAN	Pan kidney (KICH+KIRC+KIRP)	-0.787	-187.214	0.311	-20.694	-0.296	-18.711
LAML	Acute Myeloid Leukemia	-0.309	-4.447	0.538	-13.652	-0.314	-4.593
LGG	Brain Lower Grade Glioma	-0.395	-19.982	0.642	-60.501	0.139	-2.810
LIHC	Liver hepatocellular carcinoma	-0.293	-8.047	0.028	-0.227	-0.169	-2.955
LUAD	Lung adenocarcinoma	-0.291	-10.748	0.119	-2.158	-0.316	-12.690
LUSC	Lung squamous cell carcinoma	-0.300	-11.188	0.311	-11.994	-0.186	-4.533
MESO	Mesothelioma	-0.402	-3.937	0.479	-5.582	-0.347	-3.004
OV	Ovarian serous cystadenocarcinoma	-0.261	-5.379	0.422	-13.778	-0.119	-1.412
PAAD	Pancreatic adenocarcinoma	-0.466	-10.240	0.294	-4.166	-0.313	-4.691
PCPG	Pheochromocytoma and Paraganglioma	-0.313	-4.712	0.734	-30.792	-0.208	-2.293
PRAD	Prostate adenocarcinoma	-0.525	-35.783	0.481	-29.396	-0.059	-0.723
READ	Rectum adenocarcinoma	-0.435	-4.925	0.520	-7.096	-0.324	-2.847
SARC	Sarcoma	-0.253	-4.434	0.437	-12.788	-0.143	-1.664
SKCM	Skin Cutaneous Melanoma	-0.385	-4.225	0.436	-5.379	0.103	-0.523
STAD	Stomach adenocarcinoma	-0.293	-8.941	0.229	-5.611	-0.193	-4.119
STES	Stomach and Esophageal carcinoma	-0.351	-18.064	0.074	-1.142	-0.357	-18.687
TGCT	Testicular Germ Cell Tumors	-0.290	-3.499	0.304	-3.801	0.330	-4.425
THCA	Thyroid carcinoma	-0.293	-10.677	0.152	-3.192	-0.264	-8.719
THYM	Thymoma	-0.127	-0.778	0.323	-3.503	-0.068	-0.339
UCEC	Uterine Corpus Endometrial Carcinoma	-0.209	-2.273	0.403	-7.551	0.093	-0.663
UCS	Uterine Carcinosarcoma	-0.362	-2.243	0.417	-2.898	0.133	-0.491
UVM	Uveal Melanoma	-0.121	-0.548	0.318	-2.397	0.067	-0.255

b

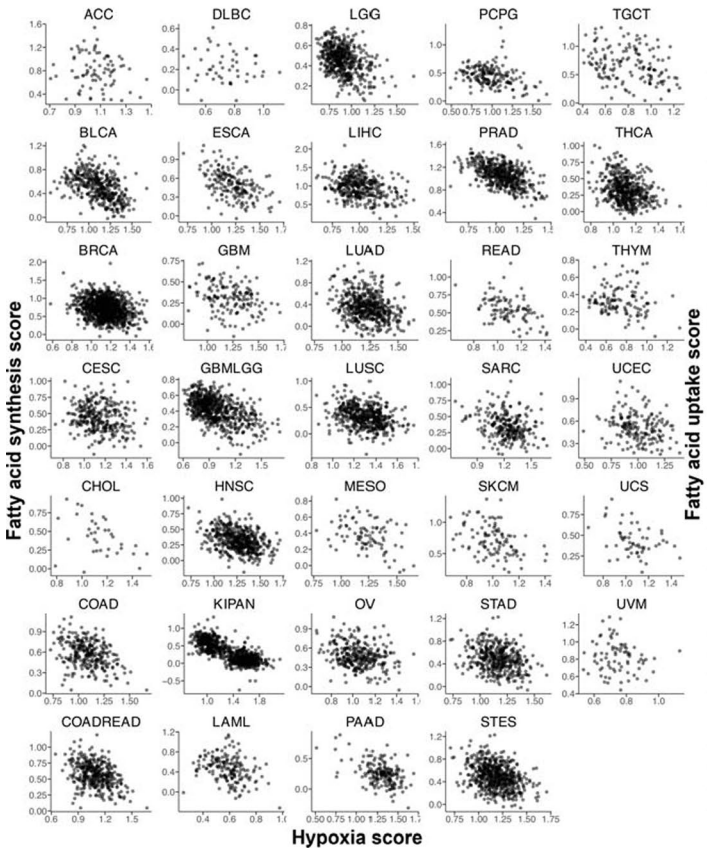

c

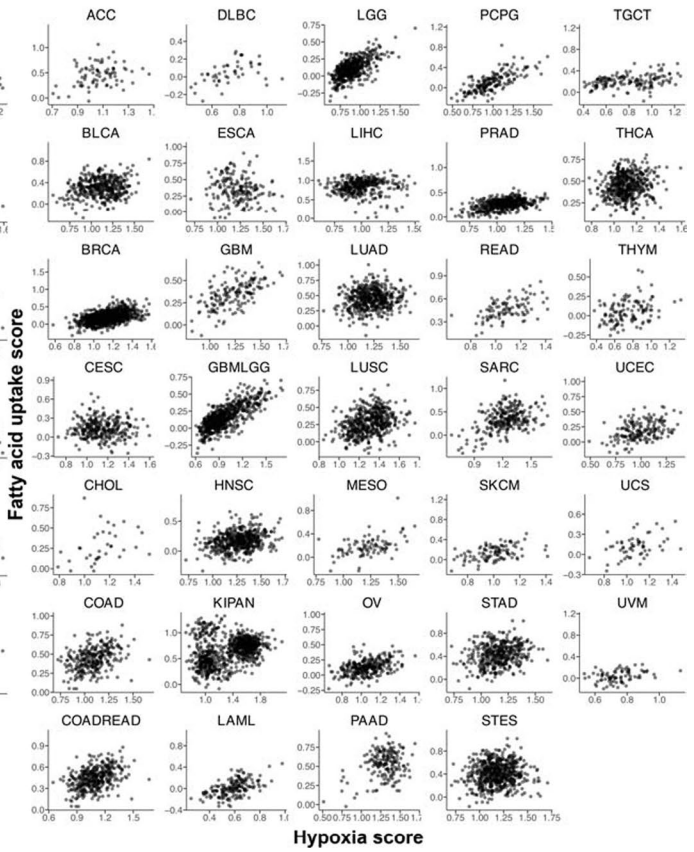

Extended Data Fig. 9 | See next page for caption.

Extended Data Fig. 9 | Gene expression correlations between lipid metabolism genes and hypoxia signature genes. a, Pearson correlation coefficients and corresponding p-values, for each of 34 different tumor types, between expression of hypoxia signature genes and expression of fatty acid synthesis genes (third column), lipid uptake genes (fourth column), and beta-oxidation genes (fifth column). Insignificant correlations, based on the 1% FDR cutoff, are marked in red. Depicted p-values on Pearson correlation coefficients are calculated using two-sided Student's *t*-test, and significance threshold is adjusted for multiple comparisons at 1% FDR using the Benjamini-Hochberg method. **b**, Scatter plots showing, for each considered tumor type, the correlation between the tumor hypoxia score and expression of genes participating in fatty acid synthesis, with dots representing individual TCGA samples. **c**, Scatter plots showing, for each considered tumor type, the correlation between the tumor hypoxia score and expression of genes participating in lipid uptake, with dots representing individual TCGA samples.

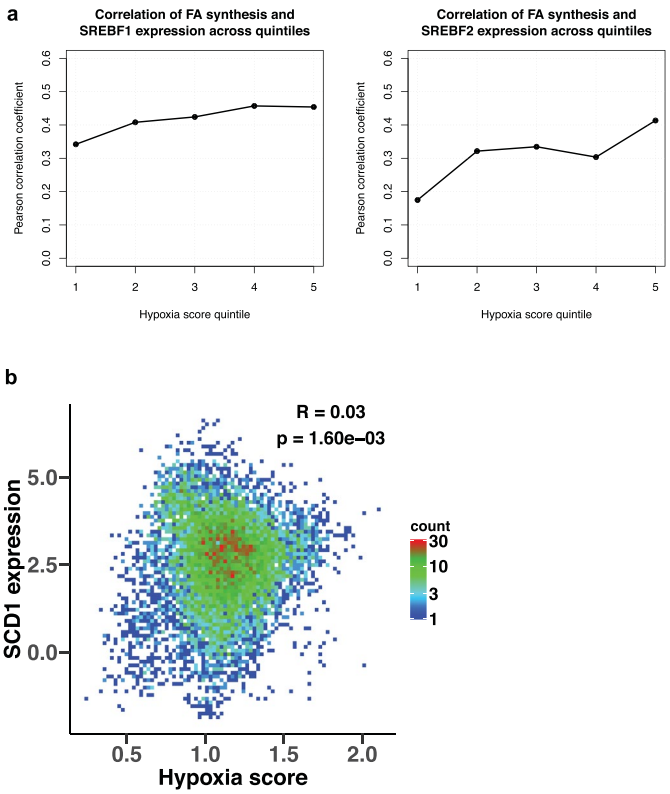

Extended Data Fig. 10 | Gene expression correlations between lipid metabolism genes and hypoxia signature genes. a, Correlation of mRNA expression of SREBF1/2 and of gene markers of fatty acid synthesis within individual hypoxia score quintiles. Pearson's correlation coefficients were calculated for each of five equally-sized bins of TCGA samples, corresponding to five hypoxia score quintiles, for SREBF1 (left) and SREBF2 (right). TCGA samples were sorted into quintiles based on their hypoxia scores from the lowest hypoxia score (quintile 1) to the highest score (quintile 5). **b**, Density plot of the correlation between the average mRNA expression of gene markers of tumor hypoxia and mRNA expression of Stearoyl-CoA desaturase 1 (SCD1) gene. Density counts represent the number of TCGA samples with the corresponding expression values, with red color representing high-density regions and blue color representing low-density regions, and the Pearson's correlation coefficient (R) and the p-value are shown in the figure. Depicted p-value on Pearson correlation coefficients is calculated using two-sided Student's *t*-test.

nature portfolio

Corresponding author(s): Dennis Vitkup and Matthew Vander Heiden

Last updated by author(s): May 12, 2022

Reporting Summary

Nature Portfolio wishes to improve the reproducibility of the work that we publish. This form provides structure for consistency and transparency in reporting. For further information on Nature Portfolio policies, see our Editorial Policies and the Editorial Policy Checklist.

Statistics

For all statistical analyses, confirm that the following items are present in the figure legend, table legend, main text, or Methods section.

n/a	Confirmed	
☐	☒	The exact sample size (*n*) for each experimental group/condition, given as a discrete number and unit of measurement
☐	☒	A statement on whether measurements were taken from distinct samples or whether the same sample was measured repeatedly
☐	☒	The statistical test(s) used AND whether they are one- or two-sided *Only common tests should be described solely by name; describe more complex techniques in the Methods section.*
☐	☒	A description of all covariates tested
☐	☒	A description of any assumptions or corrections, such as tests of normality and adjustment for multiple comparisons
☐	☒	A full description of the statistical parameters including central tendency (e.g. means) or other basic estimates (e.g. regression coefficient) AND variation (e.g. standard deviation) or associated estimates of uncertainty (e.g. confidence intervals)
☐	☒	For null hypothesis testing, the test statistic (e.g. *F*, *t*, *r*) with confidence intervals, effect sizes, degrees of freedom and *P* value noted *Give P values as exact values whenever suitable.*
☒	☐	For Bayesian analysis, information on the choice of priors and Markov chain Monte Carlo settings
☒	☐	For hierarchical and complex designs, identification of the appropriate level for tests and full reporting of outcomes
☐	☒	Estimates of effect sizes (e.g. Cohen's *d*, Pearson's *r*), indicating how they were calculated

Our web collection on statistics for biologists contains articles on many of the points above.

Software and code

Policy information about availability of computer code

Data collection	No software was used to collect data.
Data analysis	Data analysis and statistical tests were performed using Prism 8 (Graphpad). Gas chromatograph/mass spectrometry data was analyzed using a custom in-house code written in MATLAB or analyzed using m/zMine2.

For manuscripts utilizing custom algorithms or software that are central to the research but not yet described in published literature, software must be made available to editors and reviewers. We strongly encourage code deposition in a community repository (e.g. GitHub). See the Nature Portfolio guidelines for submitting code & software for further information.

Data

Policy information about availability of data

All manuscripts must include a data availability statement. This statement should provide the following information, where applicable:

- Accession codes, unique identifiers, or web links for publicly available datasets
- A description of any restrictions on data availability
- For clinical datasets or third party data, please ensure that the statement adheres to our policy

The datasets generated during and/or analysed during the current study are available from the corresponding author on reasonable request and/or are present as Source Data in the accompanied files.

Field-specific reporting

Please select the one below that is the best fit for your research. If you are not sure, read the appropriate sections before making your selection.

☒ Life sciences ☐ Behavioural & social sciences ☐ Ecological, evolutionary & environmental sciences

For a reference copy of the document with all sections, see nature.com/documents/nr-reporting-summary-flat.pdf

Life sciences study design

All studies must disclose on these points even when the disclosure is negative.

Sample size	Sample size were determined by pilot studies to establish the range of effect sizes expected from each experiment. No formal power studies were performed in determining sample size.
Data exclusions	No data were excluded from this study.
Replication	Each experiment was replicated at least 3 times by the lead experimental author. Some experiments were replicated independently by the other authors listed.
Randomization	Samples were not formally randomized in this study. When possible, samples IDs were assigned a numerical value prior to analysis.Data acquisition and analysis were largely automated and deemed to be independent of manual analysis. Covariates were controlled by performing experiments on different days.
Blinding	The investigators were not formally blinded in this study due to practical limitations of the experimental being performed and data collected/analyzed by the same researcher.

Reporting for specific materials, systems and methods

We require information from authors about some types of materials, experimental systems and methods used in many studies. Here, indicate whether each material, system or method listed is relevant to your study. If you are not sure if a list item applies to your research, read the appropriate section before selecting a response.

Materials & experimental systems

n/a	Involved in the study
☐	☒ Antibodies
☐	☒ Eukaryotic cell lines
☒	☐ Palaeontology and archaeology
☒	☐ Animals and other organisms
☒	☐ Human research participants
☒	☐ Clinical data
☒	☐ Dual use research of concern

Methods

n/a	Involved in the study
☒	☐ ChIP-seq
☒	☐ Flow cytometry
☒	☐ MRI-based neuroimaging

Antibodies

Antibodies used	Protein was detected with the primary antibodies anti-Pyruvate Dehydrogenase E1-alpha subunit (phospho S232) (EMD Millipore, AP1063), anti-Pyruvate Dehydrogenase E1-alpha subunit (phospho S293) (Abcam, ab92696), anti-Pyruvate Dehydrogenase E1-alpha subunit (phospho S300) (EMD Millipore, AP1064), anti-Pyruvate Dehydrogenase E1-alpha subunit (total) (Proteintech, 18068-1-AP), anti-PDHK1 (Cell Signaling Technologies, C47H1), anti-PDP1 (Cell Signaling Technologies, D8Y6L), anti-FASN (Cell Signaling Technologies, 3180S), anti-ACC1 (Cell Signaling Technologies, 4190S), anti-ACC1 (phospho S79) (Cell Signaling Technologies, 3661S), and anti-Vinculin (Sigma, V9131). The secondary antibody used was anti-rabbit IgG HRP-linked antibody (Cell Signaling Technologies, 7074S).
Validation	The antibodies were validated by the manufacturer as shown through immunoblot analysis on the manufacturer website(s).

Eukaryotic cell lines

Policy information about cell lines

Cell line source(s)	The cell lines A549, PANC-1, H1299, 143B, and HeLa were acquired from ATCC. The cell line AL1376 was derived from a pancreatic ductal adenocarcinoma isolated from a KP(-/-)CT [LSL-KrasG12D/+, TP53flox/flox, Pdx-1-Gre, LSL-tdTomato) mouse in a C57Bl6/J background.

Authentication	A549, PANC-1, H1299, 143B, and HeLa cells were authenticated using SNP analysis. AL1376 was authenticated using PCR analysis to asses for the KP(-/-)CT genotype.
Mycoplasma contamination	All cell lines were tested for mycoplasma contamination quarterly and confirmed to be negative.
Commonly misidentified lines (See ICLAC register)	A549 and HeLa cells were included in this study due to preexisting metabolic flux analysis being performed in this model, and thus these cells were used to validated the model predictions.